The Astrophysical Journal, 892:91 (19pp), 2020 April 1 https://doi.org/10.3847/1538-4357/ab7b60

Dusty Stellar Birth and Death in the Metal-poor Galaxy NGC 6822

Alec S. Hirschauer[1], Laurin Gray[1,2,3], Margaret Meixner[1,4], Olivia C. Jones[5], Sundar Srinivasan[6], Martha L. Boyer[1], and B. A. Sargent[1,4]
[1] Space Telescope Science Institute, 3700 San Martin Dr., Baltimore, MD 21218, USA
[2] Steward Observatory, University of Arizona, 933 N. Cherry Ave., Tucson, AZ 85721, USA
[3] Department of Astronomy, Indiana University, 727 E. 3rd St., Bloomington, IN 41405, USA
[4] Department of Physics & Astronomy, Johns Hopkins University, 3400 N. Charles St., Baltimore, MD 21218, USA
[5] UK Astronomy Technology Centre, Royal Observatory, Blackford Hill, Edinburgh, EH9 3HJ, UK
[6] Instituto de Radioastronomía y Astrofísica, UNAM. Apdo. Postal 72-3 (Xangari), Morelia, Michoacán 58089, Michoacán, México
Received 2019 December 20; revised 2020 February 25; accepted 2020 February 26; published 2020 April 1

Abstract

The nearby (∼500 kpc) metal-poor ([Fe/H] ≈ −1.2; $Z \approx 30\%\ Z_{\odot}$) star-forming galaxy NGC 6822 has a metallicity similar to systems at the epoch of peak star formation. Through identification and study of dusty and dust-producing stars, it is therefore a useful laboratory to shed light on the dust life cycle in the early universe. We present a catalog of sources combining near- and mid-IR photometry from the United Kingdom Infrared Telescope (*J*, *H*, and *K*) and the Spitzer Space Telescope (IRAC 3.6, 4.5, 5.8, and 8.0 μm and MIPS 24 μm). This catalog is employed to identify dusty and evolved stars in NGC 6822 utilizing three color–magnitude diagrams (CMDs). With diagnostic CMDs covering a wavelength range spanning the near- and mid-IR, we develop color cuts using kernel density estimate (KDE) techniques to identify dust-producing evolved stars, including red supergiant (RSG) and thermally pulsing asymptotic giant branch (TP-AGB) star candidates. In total, we report 1292 RSG candidates, 1050 oxygen-rich AGB star candidates, and 560 carbon-rich AGB star candidates with high confidence in NGC 6822. Our analysis of the AGB stars suggests a robust population inhabiting the central stellar bar of the galaxy, with a measured global stellar metallicity of $[\mathrm{Fe/H}] = -1.286 \pm 0.095$, consistent with previous studies. In addition, we identify 277 young stellar object (YSO) candidates. The detection of a large number of YSO candidates within a centrally located, compact cluster reveals the existence of an embedded, high-mass star formation region that has eluded previous detailed study. Spitzer I appears to be younger and more active than the other prominent star-forming regions in the galaxy.

Unified Astronomy Thesaurus concepts: Asymptotic giant branch stars (2100); Young stellar objects (1834); Dwarf irregular galaxies (417); Infrared photometry (792); Star forming regions (1565)

Supporting material: machine-readable table

1. Introduction

The nearby dwarf irregular galaxy NGC 6822 (Figure 1) is a well-studied member of the Local Group. At a distance of 490 ± 40 kpc (Sibbons et al. 2012, 2015), its stellar populations are resolved (Hoessel & Anderson 1986; Gallart et al. 1994; Marconi et al. 1995; Gallart et al. 1996; Komiyama et al. 2003; de Blok & Walter 2006), and with no known close companions (de Blok & Walter 2000), it is located in an isolated environment free from gravitational interactions with other systems. Possessing active star formation throughout its disk, NGC 6822 is home to some of the brightest giant H II regions known in the local universe (Hubble 1925). Spectral abundance analyses of these nebulae have yielded low metallicities (∼30% $Z_{\odot}$; Skillman et al. 1989; Lee et al. 2006), intermediate between that of the Large and Small Magellanic Clouds (LMC/SMC; Russell & Dopita 1992; Rolleston et al. 1999, 2003; Lee et al. 2005). The metal-poor nature and active star formation characteristics of NGC 6822 make it an important observationally accessible analog to the active galaxies which populated the universe at the epoch of peak star formation ($z \sim 1.5$–2; Madau & Dickinson 2014; Van Sistine et al. 2016).

As a nearby star-forming galaxy, many multiwavelength studies of NGC 6822 have been completed. Wide-field coverage of the galaxy in the optical and infrared (IR) bands have allowed for identification and classification of different stellar types. Broadband optical data in *UBVRI* was taken by Massey et al. (2007). Warm dust emission from the interstellar medium (ISM) has been characterized with the Spitzer Space Telescope (Cannon et al. 2006), while cold dust emission was described with the Herschel Space Observatory (Galametz et al. 2010). de Blok & Walter (2006) studied the H I distribution of NGC 6822, finding it to be unusually propagated much farther beyond the main optical component of the galaxy. The massive star population of NGC 6822 has been studied in detail by Bianchi et al. (2001). Carbon star candidates were previously identified by Letarte et al. (2002). Detection of RR Lyrae stars in NGC 6822 (Clementini et al. 2003; Baldacci et al. 2004) indicates the presence of an old stellar population with an age of ∼11 Gyr. The many H II regions and OB associations, however, confirm that star formation is still actively ongoing.

Photometry in the IR traces both the beginnings and ends of stellar lifetimes. Stars in the initial stages of formation radiate strongly in IR wavelengths, as light is absorbed and reemitted by cool accretion disks. These young stellar objects (YSOs) possess strong IR excesses and are generally confined in proximity to regions of active star formation (Whitney et al. 2008; Seale et al. 2009; Carlson et al. 2012; Jones et al. 2019). Evolved stars such as red supergiants (RSGs) and those populating the asymptotic giant branch (AGB) are among the brightest objects detected in the mid-IR. RSGs and AGB stars are luminous, cool, short-lived evolutionary phases of high-mass (10 $M_{\odot}$ to 30 $M_{\odot}$) and low- to intermediate-mass (0.6 $M_{\odot}$ to 10 $M_{\odot}$) main sequence (MS)

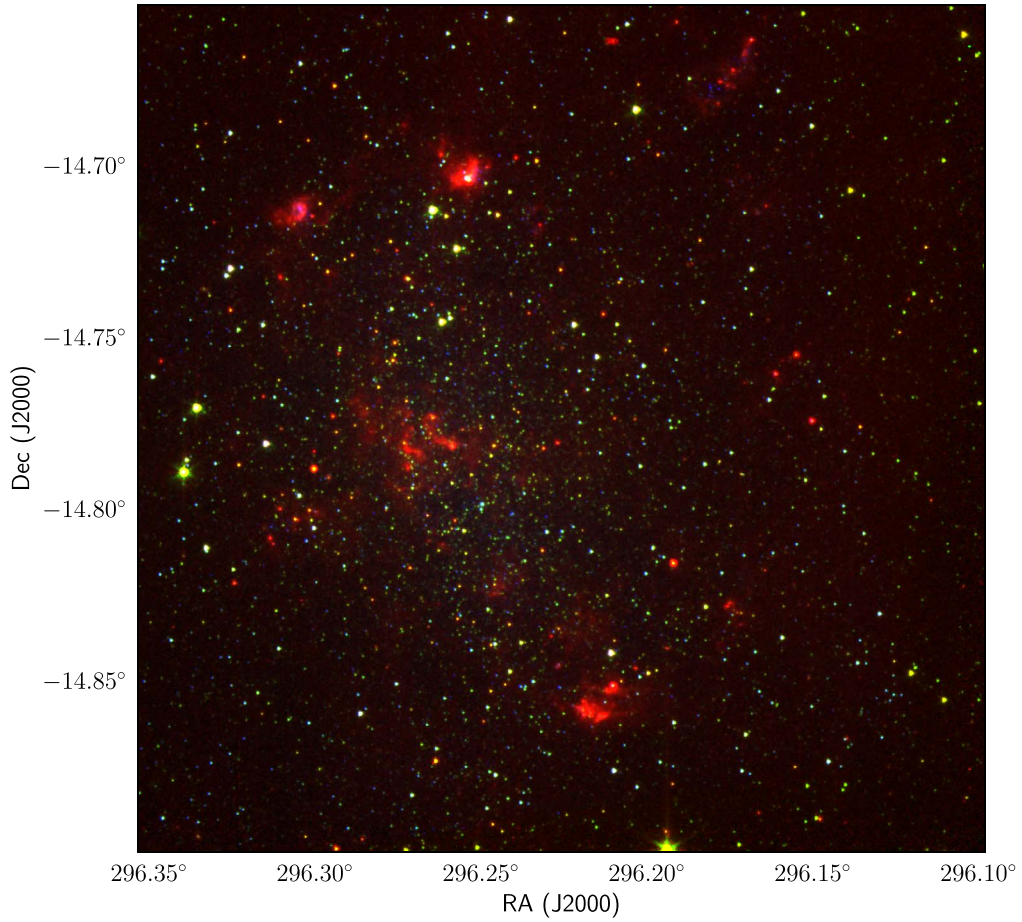

Figure 1. Composite optical and infrared (IR) image of NGC 6822. *V*-band photometry is from the Prime Focus Direct Imager on the CTIO 4 m telescope (Hunter & Elmegreen 2006), while 3.6 and 8.0 μm photometry is from Spitzer IRAC (Khan et al. 2015). This nearby dwarf irregular galaxy represents an accessible analog to the star-forming systems inhabiting the universe at higher redshifts ($z \sim 1.5$–2), useful for detailed study of star formation and chemical and dust enrichment within metal-poor environments. NGC 6822 is home to some of the brightest star-forming region complexes in the Local Group, recognizable as clumps of red emission.

progenitors, respectively. While RSGs trace recent star formation, AGB stars trace the old- and intermediate-age populations in galaxies (Blum et al. 2006). As AGB stars become more advanced in their evolution, convective cells and thermal pulsations drive enriched nucleosynthetic chemical products from the stellar interior toward and beyond the surface (Höfner & Olofsson 2018). These thermally pulsing AGB (TP-AGB) stars can manifest as rich in oxygen or carbon. While the optically thin members of this population are relatively easily separated into O- and C-rich chemistries based on their near-IR colors, the most dust-obscured TP-AGB stars (sometimes called "extreme" AGB stars; Blum et al. 2006; Boyer et al. 2011) are not similarly discernible. These objects are identified by their very red colors in longer wavelength bands. As the final evolutionary phase for the vast majority of stars that have left the MS, the contribution of mass loss from RSGs and TP-AGB stars to the ISM, and the subsequent effects of this mass loss on the evolution of both the ISM and on the stars themselves, is substantial (Höfner & Olofsson 2018).

Significant effort has been expended conducting recent searches for evolved stars in local galaxies with IR photometry. For example, the DUST in Nearby Galaxies with Spitzer survey (DUSTiNGS; Boyer et al. 2015a, 2015b, 2017; McQuinn et al. 2017; Goldman et al. 2019) presented a census of dust-producing AGB stars in a sample of 50 nearby galaxies within 1.5 Mpc in 3.6 and 4.5 μm. DUSTiNGS provided evidence that AGB stars are a major contributor of interstellar dust, even at very low metallicities. Additionally, JHK_s photometry from the WIYN High-resolution Infrared Camera at Kitt Peak studied RSGs and AGB stars in Sextans A and Leo A (Jones et al. 2018), with results supporting the DUSTiNGS findings. The current state of the art for dusty and evolved star identification in external galaxies is the Spitzer Legacy Program Surveying the Agents of Galaxy Evolution (SAGE), which imaged the LMC (Blum et al. 2006; Meixner et al. 2006; Bernard et al. 2008; Whitney et al. 2008) and the SMC (Boyer et al. 2011; Gordon et al. 2011; Sewiło et al. 2013). These programs studied the dust processes in the ISM and provided censuses of newly formed stars, to determine the current star formation rate (SFR; e.g., Seale et al. 2009; Carlson et al. 2012), and evolved stars, to quantify the dust-production and mass-injection rates into the ISM (e.g., Matsuura et al. 2009; Boyer et al. 2012; Riebel et al. 2012; Srinivasan et al. 2016). In addition, the SAGE program generated several follow-up studies, including mid-IR spectroscopic data in the LMC (SAGE-Spec; Kemper et al. 2010; Blum et al. 2014; Jones et al. 2017b) and SMC (SMC-Spec; Ruffle et al. 2015), as well as observations with the Herschel Space Telescope (HERITAGE; Meixner et al. 2010, 2013) and its follow-up studies (e.g., Jones et al. 2015).

While detailed studies of the dusty and evolved star populations within the Magellanic Clouds with SAGE are possible thanks to their close proximity and the high sensitivity afforded by *Spitzer*, for a more comprehensive understanding, we must extend our search to additional galaxies such as NGC 6822. Characterization of the oxygen- and carbon-rich populations of AGB stars across the entirety of NGC 6822 was first conducted by Cioni & Habing (2005) with the William Herschel Telescope, while the distribution of O- and C-rich AGB stars across the central bar of NGC 6822 was analyzed by Kang et al. (2006) using the Canada–France–Hawaii Telescope. The distribution of O- and C-rich AGB stars was further refined by Sibbons et al. (2012) using observations with the United Kingdom Infrared Telescope (UKIRT) and included an exploration of spatial variations in metallicity estimates. Demographics of AGB stars in NGC 6822 were refined via spectroscopic study in Groenewegen et al. (2009), Kacharov et al. (2012), and Sibbons et al. (2015), employing data from the VLT and the Anglo-Australian Telescope. Variability of the AGB star populations was studied by Battinelli & Demers (2011) and Whitelock et al. (2013) utilizing the Cerro Tololo Inter-American Observatory (CTIO) and the Japanese South-African Survey Facility (IRSF), respectively.

In this study, we utilize archival ground- and space-based near- and mid-IR photometric data of NGC 6822 in an effort to identify RSG, TP-AGB star, and YSO candidates. We have produced a catalog of sources compiled over a wide wavelength range that will be a useful resource for continuing and future investigations of the dusty stellar populations of NGC 6822. These dusty sources are representative of the very early and very late stages of stellar lifetimes, providing critically important constraint to our understanding of star formation and stellar evolution in metal-poor environments analogous to the early universe. We implement new techniques for developing our selection methods, emphasizing statistical rigor and a robust consideration of uncertainties. Our resulting color cuts inform a sophisticated algorithm for categorizing the sources into several stellar classifications, including M-type stars (O-rich AGB stars and RSGs), C-type stars (C-rich AGB stars), and YSOs. These classifications are then used to explore the spatial distribution and metallicity of the galaxy. From this work, we prepare best practices for upcoming James Webb Space Telescope (JWST) guaranteed time observation (GTO) programs which will observe NGC 6822 and other metal-poor star formation sites in the near future.

In Section 2, we describe the archival data adopted for this study and describe the characteristics of a joined master catalog of sources in NGC 6822. Section 3 introduces the color–magnitude diagrams (CMDs), kernel density estimate (KDE) techniques, and procedures employed in our source classifications, including the establishment of color-cut boundaries and populating the catalogs of stellar types. In Section 4, we explore the spatial distribution of the dusty and evolved sources within NGC 6822 as well as a preliminary investigation of the metallicity of the system. We also compare our results with previous studies found in the literature. Finally, in Section 5, we summarize our findings.

2. The Data

This project utilized archival photometric data of NGC 6822 in the near- and mid-IR. From the study of Sibbons et al. (2012), ground-based J, H, and K photometry have been adopted from the Wide Field CAMera (WFCAM) on the 3.8 m UKIRT. These data were originally obtained as part of a larger survey project of AGB stars in Local Group galaxies. Spitzer photometry ranging from 3.6 to 24 μm were adopted from Khan et al. (2015). Together, the wavelength range afforded by these two data sets provides comprehensive coverage of NGC 6822 in near- and mid-IR wavelengths, emulating the coverage anticipated with JWST. In the following subsections, we describe the individual catalogs as well as the effort undertaken to join them into a single usable resource.

2.1. UKIRT Photometry

Near-IR photometric data has been adopted from Sibbons et al. (2012), which used the Wide Field CAMera (WFCAM) on the 3.8 m United Kingdom Infrared Telescope (UKIRT) located on Maunakea to image NGC 6822 in J, H, and K. This work was completed during two runs, in 2005 April and 2006 November, as part of a larger survey project of Northern Hemisphere Local Group galaxies' AGB star content. The infrared detectors of WFCAM possess a scale of $0\farcs4$ per pixel over an observational area of 0.75 deg^2. A four-tile mosaic of 3 deg^2 centered on the optical coordinates of NGC 6822 ($\alpha = 19^{\rm h}44^{\rm m}56^{\rm s}$, $\delta = -14°48'06''$) was obtained, with combined exposure times per pixel equaling 300 seconds in J and 540 s in H and K. In total, this catalog provided near-IR data for a total of 210,979 sources.

Data reduction followed standard steps and was completed using the WFCAM pipeline at the Institute of Astronomy in Cambridge. Astrometric and photometric calibrations were performed based on the 2MASS point-source catalog (Irwin et al. 2004; Hodgkin et al. 2009). Photometric measures are based on aperture photometry, with zero points calibrated against 2MASS but not transformed into the 2MASS system, such that published magnitudes and colors are of the WFCAM instrumental system (transformation equations can be found in Hodgkin et al. 2009). Because reddening values have been found to vary across NGC 6822, with $E(B-V) = 0.24$ mag in the outer regions and $E(B-V) = 0.45$–0.54 mag in the center (Massey et al. 1995; Hernández-Martínez et al. 2009), no corrections were made for internal reddening. The extinction map of Schlegel et al. (1998) was utilized for implementing foreground component corrections.

2.2. Spitzer Photometry

We have adopted Spitzer (Werner et al. 2004) mid-IR photometric data from Khan et al. (2015), who utilized archival photometric data (Khan et al. 2010, 2013) originally employed to target stars of certain subclasses with specific photometric properties. The more recent study was designed to inventory all point sources, in effort to study seven nearby galaxies with recent star formation using the Infrared Array Camera (IRAC; Fazio et al. 2004) at 3.6, 4.5, 5.8, and 8.0 μm and the Multiband Imaging Photometer (MIPS; Rieke et al. 2004) at 24 μm. This catalog contains in total 30,745 point sources from NGC 6822, created by dual-band selection of sources with $>3\sigma$ detections within a matching radius ($<$0.5 pixels or 0.5–1.0 pixel; 90% of 4.5 μm sources match to a 3.6 μm source within 0.5 pixels) at both 3.6 and 4.5 μm, complemented with measurements of the 5.8, 8.0, and 24 μm bands through a combination of PSF and aperture photometry. It was developed as a resource archive for studying mid-IR-luminous sources and transients, as well as for planning observations with JWST, which will provide much deeper observational power than

Spitzer. With a resolution nearly an order of magnitude better than that of Spitzer (Gardner et al. 2006), data from JWST will also benefit from reduced confusion.

This catalog is ideal for identifying dusty sources in NGC 6822. With similar Spitzer IRAC band coverage, complemented with the 24 μm MIPS band, the Khan et al. (2015) source list enables a similar wavelength range of study to SAGE. It provides the J2000.0 coordinates (R.A. and decl.) for each object, along with their Vega-calibrated apparent magnitudes (m_λ), the associated 1σ uncertainties (σ_λ), and for the 3.6–8.0 μm bands, the differences between the PSF and aperture photometry magnitudes (δ_λ). Khan et al. (2015) note that, for the 24 μm band photometry, the lower spatial resolution suggests limited utility, such that the relevant aperture can be contaminated by cold interstellar dust emission and objects other than the intended target.

2.3. The Joined Catalog

In an effort to identify dusty sources in NGC 6822, we have combined the near- and mid-IR catalogs adopted from Sibbons et al. (2012) and Khan et al. (2015), respectively, into a joined master catalog. We use the CDS crossmatch utility[7] to find the nearest Sibbons et al. (2012) neighbor to each of the 30,745 sources in the Khan et al. (2015) table within a $1''$ radius. We obtain near-IR counterparts for 14,534 sources. This is a very small fraction of the full Sibbons et al. (2012) source list, due to the large difference in survey areas between the two studies. The near-IR counterparts include 1735 sources classified by Sibbons et al. (2012) as AGB stars (1099 M type, 636 C type). The $1''$ radius allows us to recover all but nine (six M type, three C type) of the Sibbons et al. (2012) AGB candidates within the *Spitzer* footprint. Table 1 describes the columns in the joined catalog, and the full catalog is available in electronic form with this paper. *JHK* photometry adopted from Sibbons et al. (2012) is presented in the WFCAM instrumental system; equations to convert to the 2MASS system are given in Hodgkin et al. (2009).

Table 1
Numbering, Names, and Description of the Columns Present in the Master Catalog

Column	Name	Description
1	ID_MIR	Unique identifier for mid-infrared source
2	RAJ2000_MIR	J2000 R.A. of mid-infrared source
3	DEJ2000_MIR	J2000 decl. of mid-infrared source
4	m_3.6	IRAC 3.6 μm magnitude
5	e_m_3.6	Uncertainty in IRAC 3.6 μm magnitude
6	m_4.5	IRAC 4.5 μm magnitude
7	e_m_4.5	Uncertainty in IRAC 4.5 μm magnitude
8	m_5.8	IRAC 5.8 μm magnitude
9	e_m_5.8	Uncertainty in IRAC 5.8 μm magnitude
10	m_8.0	IRAC 8.0 μm magnitude
11	e_m_8.0	Uncertainty in IRAC 8.0 μm magnitude
12	m_24	MIPS 24 μm magnitude
13	e_m_24	Uncertainty in MIPS 24 μm magnitude
14	ID_NIR	Unique identifier for nearest-neighbor near-infrared source
15	RAJ2000_MIR	J2000 R.A. of nearest-neighbor near-infrared source
16	DEJ2000_MIR	J2000 decl. of nearest-neighbor near-infrared source
17	distArcsec	Distance in arcseconds to nearest-neighbor near-infrared source
18	Jmag	*J*-band magnitude of nearest-neighbor near-infrared source
19	e_Jmag	Uncertainty in *J*-band magnitude of nearest-neighbor near-infrared source
20	Hmag	*H*-band magnitude of nearest-neighbor near-infrared source
21	e_Hmag	Uncertainty in *H*-band magnitude of nearest-neighbor near-infrared source
22	Kmag	*K*-band magnitude of nearest-neighbor near-infrared source
23	e_Kmag	Uncertainty in *K*-band magnitude of nearest-neighbor near-infrared source
24	Sibbons_AGB_Type	AGB classification from Sibbons et al. (2012; "M" or "C")

Note. *JHK* photometry adopted from Sibbons et al. (2012) is presented in the WFCAM instrumental system; equations to convert to the 2MASS system are given in Hodgkin et al. (2009). An addendum to this table with CMD categorizations (see Section 3.2) and final type classifications (see Section 3.3) is presented as Table 5.

(This table is available in its entirety in machine-readable form.)

3. Source Classification

In order to identify and classify the dusty and evolved stars of NGC 6822, we have created three CMDs which utilize photometry from one or both archival catalogs: K versus $J-K$ (hereafter "CMD1"; Figure 2, left), [3.6] versus $J-$[3.6] (hereafter "CMD2"; Figure 2, center), and [8.0] versus [3.6]–[8.0] (hereafter "CMD3"; Figure 2, right). These three CMDs were selected as representative of the wavelength ranges characteristic of each of the archival data sets (CMD1 and CMD3), as well as one which utilizes photometric data spanning both the near- and mid-IR wavelength regimes (CMD2). CMD1 and CMD2 show distinct features that have been described in previous studies of evolved stellar populations in nearby galaxies (e.g., Blum et al. 2006; Boyer et al. 2011; Jones et al. 2017a). Foreground objects form an almost vertical pattern in these CMDs. The RSGs are at slightly redder colors, followed by the massive O-rich AGB stars. The feature subsequently extending diagonally to redder colors consists of C-rich AGB stars, while beyond that are found highly evolved AGB stars of both chemical types (the so-called "extreme AGB" stars) and YSOs. The emission at 8 μm is dominated by the dustiest objects, which explains the difference seen in CMD3. At the faint end, the dusty AGB population suffers contamination from background galaxies and YSOs.

These three CMDs have been routinely used to devise color cuts to identify regions occupied by foreground stars, evolved stars, YSOs, and background galaxies (e.g., Boyer et al. 2011), and the resulting classifications are found to be consistent with spectroscopic identifications (e.g., Kemper et al. 2010; Jones et al. 2017a). Given the large sample size, the population boundaries can, in principle, be determined statistically using the observed density distribution in CMD space. To date, however, the color cuts have been determined largely by visual estimation alone.

In this paper, we present the first semiautomated selection criteria that use knowledge of the density distribution of various populations in CMD space. Such a method has been successfully used in the literature to compute the magnitude of

[7] http://cdsxmatch.u-strasbg.fr/xmatch

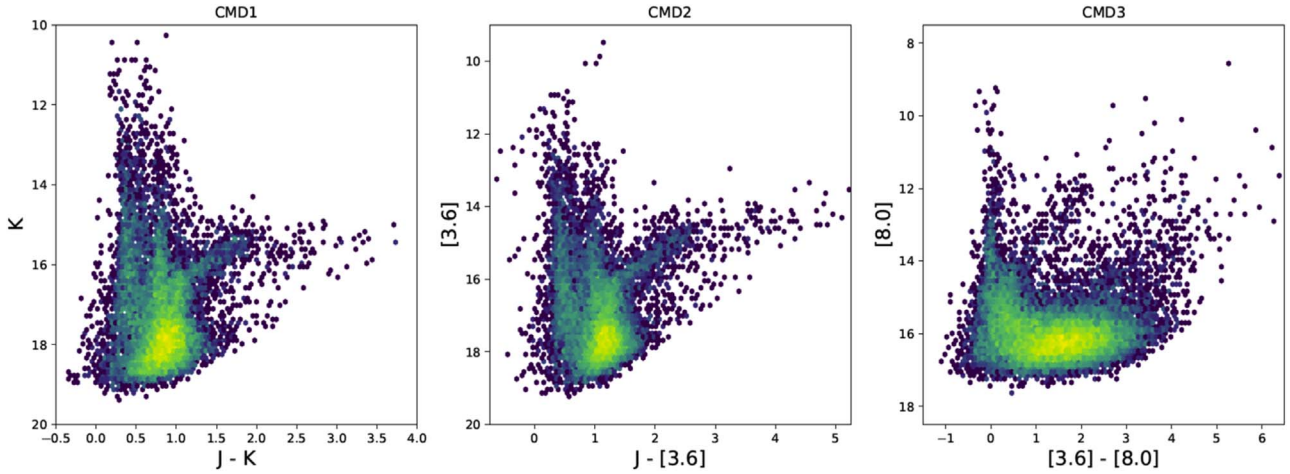

Figure 2. Hess diagrams of the three diagnostic CMDs used in this study. Photometric data for CMD1 (left; K vs. $J-K$) are taken only from Sibbons et al. (2012). Photometric data for CMD2 (center; [3.6] vs. $J-$ [3.6]) are taken from both Sibbons et al. (2012) and Khan et al. (2015). Photometric data for CMD3 (right; [8.0] vs. [3.6]–[8.0]) are taken only from Khan et al. (2015). Color cuts employing catalogs of these near- and mid-IR sources are established via KDE analyses of small, successive spans of magnitude and color.

the tip of the red giant branch (TRGB). Cioni et al. (2000) use a histogram of the density of sources near the TRGB, finding the location where the second derivative has a maximum. We refer the reader to Appendix A of Cioni et al. (2000) for an excellent background on the subject, as well as references to other authors who have used similar techniques.

As histograms come with their own problems (e.g., choice of bin sizes and bin locations; see Sections 4.8.1 and 6.1.1 in Ivezić et al. 2014), an alternative is to smooth the observed distribution without binning. In this paper, we use kernel density estimates (KDEs) to smooth our data and the local minima in these smoothed distributions to determine the boundaries between different source types in a consistent fashion. A similar method was used by Sakai et al. (1996) to determine the location of the TRGB in Sextans A. A more recent example using smoothed distributions to compute TRGB locations is the work of Freedman et al. (2019).

Utilizing the three CMDs generated from our matched catalog, we identify dusty and evolved star candidates via color cuts. In this study, we present classifications for four types of dusty and evolved stars: RSGs, oxygen-rich AGB stars, carbon-rich AGB stars, and dust-enshrouded stars (including YSOs). In addition, we identify MS stars and background galaxies; however, we emphasize that our selection techniques are not optimized for these types of objects. Our color cuts are computed by tracing the location of the local minima in kernel density estimates of the distribution in color–magnitude space. We explain this procedure in the following sections.

3.1. Determining the Tip of the Red Giant Branch

Our first step in source classification is to compute the location of the TRGB. This is an important step in the identification of dusty and evolved star candidates. This prominent feature in the magnitude distributions of old- and intermediate-aged stellar populations corresponds to a conspicuous discontinuity between RGB and AGB populations (Salaris & Girardi 2005; Sibbons et al. 2012; Madore et al. 2018). From the Padova stellar evolution models (Marigo et al. 2008, 2013), the study of Bruzual et al. (2013) created simple stellar population models of the Magellanic Clouds, finding that >90% of TP-AGB stars are brighter than the TRGB (Boyer et al. 2015a). Establishing the location of the TRGB is therefore useful as a first-order boundary used to segregate nondusty and nonevolved stars from our overall joined sample.

We determined the location of the TRGB using a KDE technique. The overall distribution of the magnitudes of all sources with photometric errors less than 0.1 mag is modeled using a Gaussian kernel via the `Gaussian_kde` module available in the Python `SciPy` library. In order to find the position of the TRGB in magnitude space, we compute the smoothed first derivative of the KDE by applying a Savitsky–Golay filter. We then identify the location of the minimum in the derivative with the location of the TRGB. In order to estimate the uncertainty associated with this estimate, we draw a large number of samples of the entire distribution using the photometric uncertainties. The results of this Monte Carlo + KDE (MCKDE) method are shown for CMD1 and CMD2 in Figure 3 as blue curves; the discontinuity between RGB and AGB populations is discernible as the point of steepest slope. The value of the derivatives to the fits is represented as red curves for both CMD1 and CMD2 in Figure 3. Where the absolute value of this curve is maximized corresponds to where in magnitude space lies the location of the separation between RGB and AGB stars, represented by the vertical green line.

For statistical robustness, the location of the TRGB was determined via Savitsky–Golay filter analysis by iterating the process 1000 times for each CMD in order to find the mean value. These superimposed results are illustrated as Figure 3 for both CMD1 and CMD2. (Because of the complexity associated with the different structure of CMD3, a TRGB was not similarly determined for it; more details in Section 3.2.) This Monte Carlo method of the KDE method (hereafter "MCKDE") provides the final value of the TRGB as well as a robust estimate of its uncertainty. For CMD1, the MCKDE method determined the TRGB at $K = 17.36 \pm 0.04$ mag (see Figure 3, left), while for CMD2, the TRGB was found to be [3.6] $= 17.16 \pm 0.06$ mag (see Figure 3, right).

3.2. Establishing Color-cut Boundaries

The distribution of sources in each of the three CMDs presents structure representative of the underlying stellar astrophysics (Woods et al. 2011; Ruffle et al. 2015; Jones et al. 2017b). For a

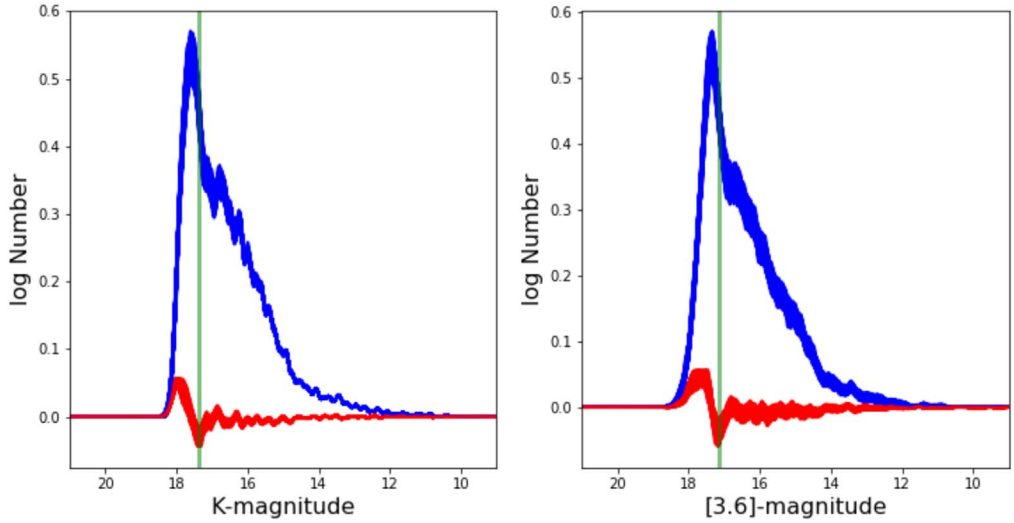

Figure 3. Our Monte Carlo + KDE method ("MCKDE") provides both the location of and the uncertainty associated with the TRGB for CMD1 (left; $K = 17.36 \pm 0.03$ mag) and CMD2 (right; $[3.6] = 17.15 \pm 0.06$ mag), indicated with vertical green lines. Each MCKDE routine encompasses 1000 realizations of a Gaussian kernel fit and Savistky–Golay filter applied to the respective distribution of sources. The location of the TRGB is determined as the point along the *x*-axis where the slope of the KDE fit to the data (blue line) is steepest. Here, the absolute value of the red line (representing the magnitude of the derivative) is maximized, corresponding to the discontinuity between RGB and AGB stars.

given individual source, the combination of magnitude and color reflects both the physical properties and current evolutionary phase of the star. Such parameters are generally not obviously and easily demarcated along lines of constant magnitude or color. The spur of points extending up and to the right from the main clustering of sources in both CMD1 and CMD2, for example, cannot be well isolated and categorized through strictly vertical and horizontal demarcating boundary lines (e.g., Nikolaev & Weinberg 2000; Weinberg & Nikolaev 2001; Cioni & Habing 2005; Blum et al. 2006; Cioni et al. 2006; Boyer et al. 2011, 2015c). These clustered points in color–magnitude space clearly represent a distinct stellar type.

The presence of opacity differences, as well as underlying absorption features from various molecular bands and dust, have a profound effect on the photometric properties of the various stellar types. Consequently, these populations become grouped together on the diagnostic CMDs, making it possible to distinguish them from one another. For example, C-rich stars appear red due in part to characteristic C_2 bands between 1.15 and 1.3 μm (Groenewegen et al. 2009), as well as HCN and C_2H_2 absorption features at 3.5 and 3.8 μm within the Spitzer IRAC 3.6 μm band (Marengo et al. 2007). In the IRAC 8.0 μm band, silicate features such as SiO and SO_2 are prominent in O-rich evolved stars, as they are quite sensitive to the amounts of dust being produced. For the near-IR, Wright et al. (2009) present a catalog of AGB star absorption features from molecular bands useful for modeling integrated emission for evolved stars. In addition, Blum et al. (2006) showed that, utilizing star formation history models of the LMC using the 2MASS CMD from Cioni et al. (2006) and new stellar models from Marigo et al. (2003), C- and O-rich AGB stars were well defined and separated in their CMDs (similar to the ones used in this study). A strategy to group such sources under one classification which more closely resembles these structures of points is therefore to define boundaries which follow the natural shape and direction seen in the diagrams.

In order to define such boundaries between stellar types in color space, we implemented KDE analyses of the distribution of sources in each of the three CMDs. With the location of the TRGB established for CMD1 and CMD2, small successive spans of magnitude incorporating at least 1000 points (for statistical robustness) were defined to progressively lower magnitude. The vertically stacked magnitude spans used in the analyses of CMD1 and CMD2 are sufficiently capable of separating the different stellar types (see Figure 4, left and center, respectively). Establishment of color-cut boundaries for CMD3, however, required supplemental restraint, due to its more complicated structure. Notably, the separation between some stellar types, particularly that which segregates background galaxies from dusty sources, run horizontally across the CMD. Because this direction runs congruent with the magnitude-only spans from which the boundary lines are derived, it is difficult for the KDE procedure to determine an optimal border location. In addition to vertically stacked magnitude spans, we therefore additionally implemented horizontally stacked spans in color space, again possessing a minimum 1000 sources. With a comparison of the demarcation lines defined by both the vertically stacked color spans and horizontally stacked magnitude spans, we define functional fits to the segregation boundaries of this longer wavelength CMD (see Figure 4, right).

In each of these spans of magnitude (and/or color for CMD3), a KDE fit was established (see Figure 5, left) which defined the shape of the distribution of sources (see Figure 5, right). In the left plot of this figure, within the boundaries of the CMD established by the red lines, the blue points represent only the data within the given range. We note that some points in the magnitude ranges are not included in the KDE analysis (i.e., left as gray in the plots) as they introduced unnecessary noise to the fit that had no effect on the results. In the right plot of this figure, a histogram of the data (blue columns) is presented as comparison with the KDE fit (black line). Where the fit presents a local minimum is coincident with gaps in the histogram. Locations of the local minima in each span are representative of breaks in the numbers of various stellar populations and are therefore representative of the physically

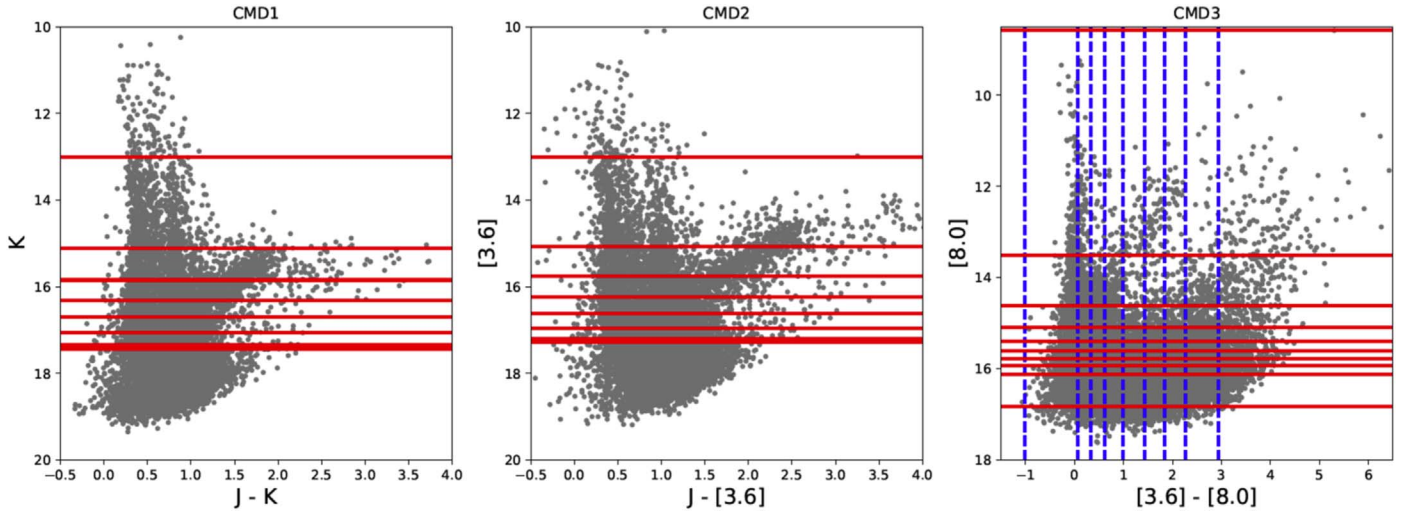

Figure 4. Successive magnitude spans utilized for each of the three diagnostic CMDs of this study. For each of these magnitude spans, containing at least 1000 points, KDE minima analyses determine where there exist separations between distinct stellar types. CMD1 and CMD2 (left and center) employ only vertically stacked spans of successive magnitude (red lines), while CMD3 (right) required both vertically stacked (red solid lines) and horizontally stacked (blue dashed lines) spans of magnitude and color, as its structure is more complicated. Color cuts were subsequently established based on the combined results. For CMD1 and CMD2, the TRGB is identified as the thicker red line ($K = 17.36 \pm 0.04$ and $[3.6] = 17.16 \pm 0.06$, respectively).

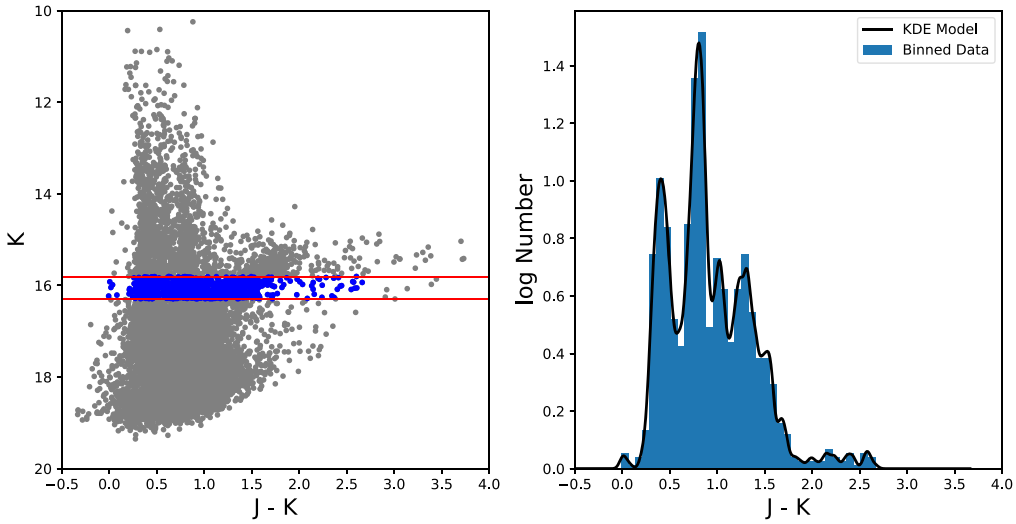

Figure 5. Example magnitude span from CMD1 (left; $K = 16.316$–15.846) and a histogram and KDE fit to the data (right). Red lines indicate the magnitude range for this particular span, while blue dots represent only the data within this range. Gray points are outside the considered range. Local minima in the KDE are representative of distinctive breaks in numbers of various stellar populations. For each magnitude span, local minima of the central y-value indicate where in $J-K$ space (on the x-axis) a boundary between the different kinds of stars exists. Summing the locations of these minima along the successive magnitude spans indicates where the color-cut boundaries should be placed. This KDE local minima analysis technique was implemented for determining all color cuts.

distinct separations which exist between different stellar types. When these local minima from the contiguous successive magnitude spans are joined, rough demarcation lines are formed (see Figure 6). Linear fits made to these points establish the functional forms of the color-cut boundaries which were used to classify the sources in NGC 6822.

These categorizations, illustrated in Figure 7, include MS stars (Region 1; violet dots), RSGs (Region 2; gray dots), O-rich AGB star candidates (Region 3; blue dots), C-rich AGB star candidates (Region 4; red dots), dust-enshrouded AGB star and YSO candidates (Region 5; green dots), and background galaxies (Region 6; gold dots). Stellar type categorizations used here should be considered as approximations drawn from a statistical sample of sources. Furthermore, intrinsic variations of individual objects will cause some overlap. A small degree of contamination between regions is to be expected in the diagnostic CMDs. Final classification criteria implement region designations from multiple CMDs, which helps to reduce erroneous misidentifications (see Section 3.3 for details). In addition, we are not able to take into account the myriad variety of all possible stellar types. For example, short-lived blue core helium-burning sequence stars (BHeBs; also referred to as "blue loop") present a potential source of contamination at shorter wavelengths (Regions 1 and 2; Dalcanton et al. 2009). Inspection of Hubble Space Telescope (HST) data from Holtzman et al. (2006) indicates that BHeB contamination is no more than a few percent. Finally, we note that any foreground sources are most likely Galactic MS stars, and therefore are also expected to appear within shorter-wavelength regions. While some foreground stars will contaminate Region 2, we expect the

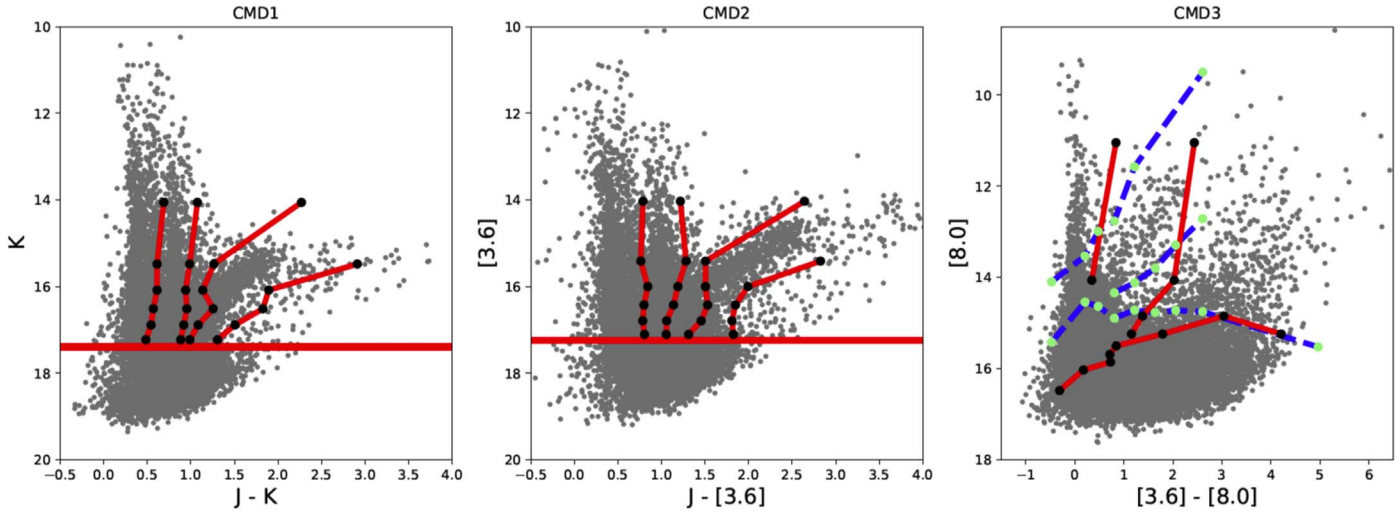

Figure 6. Boundaries separating the various stellar types in each of the three diagnostic CMDs as determined by KDE local minima analyses. For each small span in magnitude or color, the local minima found (see Figure 5) indicates where stellar populations diverge. Connecting these minima for the successive magnitude spans is then used to establish functional fits which represent the color-cut boundaries. For CMD1 and CMD2 (left and center, respectively), the red lines are derived from vertically stacked magnitude spans (the horizontal line represents the TRGB), while locations of the local minima are represented by black dots. For CMD3 (right), the red solid lines are derived from vertically stacked magnitude spans while the blue dashed lines are derived from horizontally stacked spans of color. The local minima are represented by black and green dots, respectively. Synthesizing both the vertically and horizontally stacked spans' KDE local minima into coherent color cuts required special attention to detail.

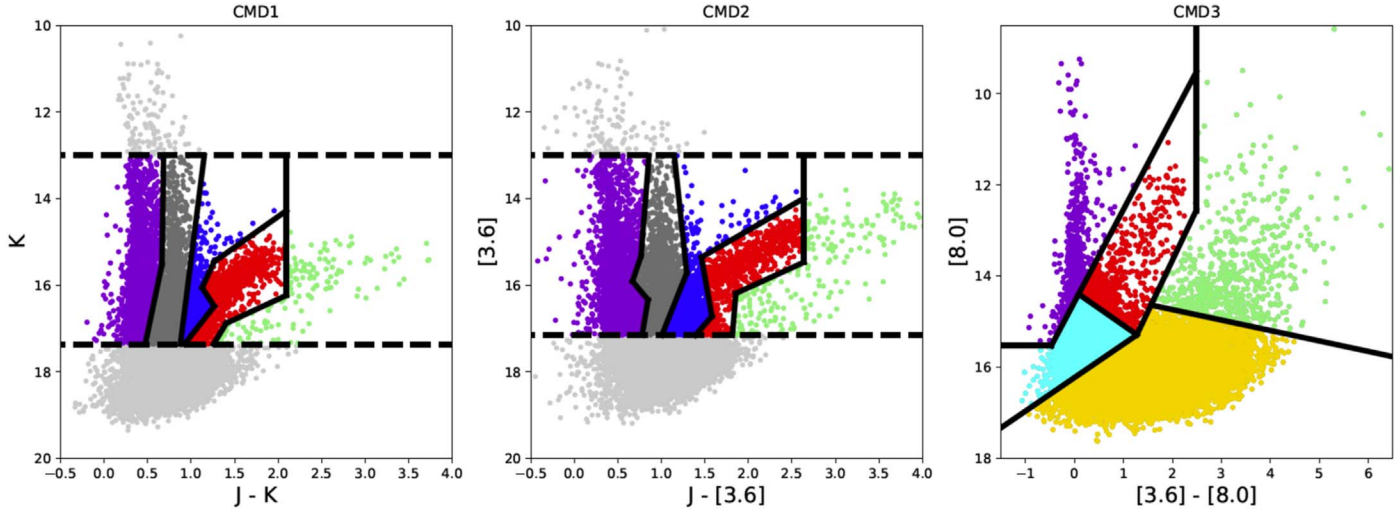

Figure 7. Color-cut boundaries (black lines) and stellar type classifications determined from each of the three diagnostic CMDs. Violet dots are foreground/MS stars, dark gray dots are RSGs (CMD1 and CMD2 only; left and center, respectively), blue dots are O-rich AGB star candidates (CMD1 and CMD2 only; left and center, respectively), cyan points are all M-type stars, including both RSG and C-rich AGB star candidates (CMD3 only; right), red dots are C-rich AGB star candidates, green dots are dust-enshrouded AGB stars and YSOs, gold dots represent background galaxies (CMD3 only; right), and light gray dots represent unclassed objects. Due to large photometric uncertainties in CMD3 below [8.0] $\approx$ 16, it is difficult to eliminate cross contamination between the cyan and gold points as CMD features become less discernible. While the gold points are dominated by background galaxies, they may also include M-type stars and YSOs.

majority to fall within Region 1. Henceforth, objects identified within this region in any CMD will be referred to collectively as "foreground/MS stars."

For CMD1 and CMD2, the color-cut boundaries are confined within the TRGB boundaries established in Section 3.1, corresponding to $K = 17.36$ mag and $[3.6] = 17.16$ mag, respectively. In addition, a second boundary for both CMD1 and CMD2 exists at K and [3.6] values of 13.0 mag, whereby the number density of sources becomes too low for KDE bins to effectively constrain the source distributions. The functional coefficients for the boundary lines separating the different stellar types in CMD1 are presented in Table 2 and are illustrated in Figure 7 (left). CMD2, which incorporates a combination of near- and mid-IR photometry, presents a distribution of sources similar in appearance to that of CMD1, but exhibits some distinct differences. Boundary-line functional coefficients which segregate the different stellar types are presented in Table 3 and are illustrated in Figure 7 (center). Finally, utilizing only mid-IR data from Spitzer IRAC bands, CMD3 presents a structure visibly different from those seen with CMD1 and CMD2. Rather than establishing a boundary line at the TRGB, color cuts were defined through analysis of KDE local minima analyses in both vertically and horizontally stacked spans of magnitude and color space, respectively. This produced the complicated set of functional fits

Table 2
Stellar Type Category Boundary Function Coefficients for CMD1, Following the Form $K = m \times (J - K) + b$

Regions Separated by Boundary Line	Slope m	y-intercept b	Left Extent $(J - K)=$	Right Extent $(J - K)=$
1 and 2	−9.586	21.892	0.472	0.665
	−128.318	100.790	0.665	0.684
2 and 3	−15.880	31.275	0.876	1.151
3 and 4	−2.568	19.735	0.923	1.265
	3.094	12.572	1.265	1.267
	−4.380	20.994	1.127	1.264
	−1.420	17.253	1.264	2.094
4 and 5	−3.301	21.511	1.257	1.403
	−0.934	18.189	1.403	2.094
	∞	⋯	2.094	2.094

Note. A slope of ∞ is representative of a vertical line.

Table 3
Stellar Type Category Boundary Function Coefficients for CMD2, Following the Form $[3.6] = m \times (J - [3.6]) + b$

Regions Separated by Boundary Line	Slope m	y-intercept b	Left Extent $(J-[3.6])=$	Right Extent $(J - [3.6])=$
1 and 2	−12.033	26.524	0.779	0.847
	2.388	14.315	0.847	0.668
	−5.969	19.898	0.668	0.766
	−25.236	34.656	0.766	0.858
2 and 3	−5.025	22.208	1.005	1.291
	19.022	−8.849	1.291	1.149
3 and 4	−2.287	20.335	1.390	1.581
	11.269	−1.095	1.581	1.460
	−1.158	17.046	1.460	2.637
4 and 5	−24.317	61.302	1.816	1.855
	−0.922	17.901	1.855	2.637
	∞	⋯	2.637	2.637

necessary to demarcate the various stellar types (see Figure 7, right). Functional coefficients of the stellar type boundary lines are presented in Table 4.

The stellar classification categories established from our analyses are presented in Table 5. These columns represent an addendum to the master joined catalog (Table 1) and are included as part of the downloadable data set. The full overall data set is available in electronic, machine-readable format. Included are an object ID number, the R.A. and decl. coordinates from Sibbons et al. (2012), and the coordinate disparity between the UKIRT and Spitzer photometry measured in arcseconds, where applicable. The Khan et al. (2015) data (Spitzer [3.6], [4.5], [5.8], [8.0], and [24]) present Vega-calibrated apparent magnitudes (m_λ) and the associated 1σ uncertainties (σ_λ) For the 5.8, 8.0, and 24 μm bands, a 1σ uncertainty of "−9999" corresponds to the photometric flux being a 3σ upper limit. Sibbons et al. (2012) data (UKIRT J, H, and K) were calibrated astrometrically and photometrically to the 2MASS point-source catalog (Irwin et al. 2004; Hodgkin et al. 2009). Photometric measurements are based on aperture photometry, using zero points calibrated against (but not transformed into) the 2MASS system.

Finally, for each source in the master joined catalog, we include an identifier value signifying the color-cut region within which the source is located for each of the three diagnostic CMDs (see Section 3.2). As with the CMD classification regions of Figure 7,

Table 4
Stellar Type Category Boundary Function Coefficients for CMD3, Following the Form $[8.0] = m \times ([3.6]–[8.0]) + b$

Regions Separated by Boundary Line	Slope m	y-intercept b	Left Extent $([3.6]–[8.0])=$	Right Extent $([3.6]–[8.0])=$
1 and 2/3	0	15.529	∞	−0.475
	−2.029	14.565	−0.475	2.485
	∞	⋯	9.522	9.522
2 and 3	0.749	14.332	0.084	1.273
2 and 6	−0.735	16.226	∞	1.273
3 and 5/6	−2.251	18.151	1.273	2.485
	∞	⋯	12.556	12.556
5 and 6	0.229	14.277	1.562	∞

Table 5
Addendum to Master Catalog (Table 1) with CMD Categorizations and Final Type Classifications

Column	Name	Description
25	CMD1	Region categorization for CMD1
26	CMD2	Region categorization for CMD2
27	CMD3	Region categorization for CMD3
28	TYPE	Final type classification

"1" signifies that the source is located in the color-cut region of foreground/MS stars. "2" represents RSG candidates, while sources marked "3" belong to O-rich AGB star candidates. C-rich AGB star candidates are notated with "4," while "5" are dust-enshrouded sources which include dusty AGB stars and YSOs. Finally, sources marked "6" are background galaxy candidates, and any object denoted as "−9999" were not classified in the given CMD (did not inhabit an available color-cut boundary region). The final column, "TYPE," gives the source classification as defined by the procedure outlined in Section 3.3. "RELIABLE" classifications are denoted by one of the following descriptors: "RSG," "O-rich," "C-rich," or "YSO." Furthermore, "CANDIDATE" sources are indicated as "RSG?," "O-rich?," "C-rich?," or "Dusty?." In addition, we note "Star," "Galaxy," and "Unclassifiable" sources based on the categorizations provided by our CMD analyses, though we note that our selection criteria are not specified for these kinds of objects. Finally, sources for which a classification was not established are presented as "Classless!."

3.3. Catalogs of Stellar Types

From the established color-cut boundaries, we have designated a type classification for every source in each of the three CMDs (see Figure 7). Guided by the KDE analyses described in the previous section, the demarcation lines indicate whether a given source is:a foreground/MS star (Region 1; violet points); an RSG candidate (Region 2 (CMD1 and CMD2 only); gray points); an O-rich AGB star candidate (Region 3 (CMD1 and CMD2 only); blue points); a C-rich AGB star candidate (Region 4; red points); a dust-enshrouded star, typical of extreme AGB star candidates and YSOs (Region 5; green points); or a background galaxy (Region 6 (CMD3 only); gold points). For CMD3 only as well, Region 2 (cyan points) corresponds to all M-type stars, which include both RSGs and O-rich AGB star candidates. If a source fails to be categorized within any of the regions described above, it is left as classless

Table 6
CMD Color-cut Initial Source Classifications

CMD	Stellar Type	Number of Sources
K versus $J-K$	RSG	2075
K versus $J-K$	O-rich AGB	1002
K versus $J-K$	C-rich AGB	907
K versus $J-K$	Dust-enshrouded	144
[3.6] versus $J-$ [3.6]	RSG	1571
[3.6] versus $J-$ [3.6]	O-rich AGB	1545
[3.6] versus $J-$ [3.6]	C-rich AGB	713
[3.6] versus $J-$ [3.6]	Dust-enshrouded	230
[8.0] versus [3.6] − [8.0]	M-type stars	2949
[8.0] versus [3.6] − [8.0]	C-rich AGB	674
[8.0] versus [3.6] − [8.0]	Dust-enshrouded	630

(represented as faint gray points in CMD1 and CMD2 of Figure 7).

The stellar type classification demographics derived from each of the three CMDs are presented in Table 6. Remarkably, the stellar type demographics from the analyses of each CMD produce numbers which are generally self-consistent. This is true despite the KDE analyses for each of the three CMDs being completed entirely independently of one another. The only obvious exception is the elevated number of dust-enshrouded sources identified in CMD3 as compared to CMD1 and CMD2. This disparity is attributable to the longer wavelengths of the photometric bands employed, resulting in an increased sensitivity to the dusty objects which primarily emit in this range.

Utilizing the stellar type categorizations as determined by each CMD individually, an overall classification for every source in the master catalog was determined. These compared the categorization results from each CMD to those from each of the other two CMDs in an effort to reach a consensus. High-confidence classifications by robust combinations of individual CMD results were classified as "RELIABLE," while lower-confidence classifications were marked as "CANDIDATE." From a total overall catalog of $N = 30{,}745$ sources, $n = 3179$ (10.3%) have been classified as a "RELIABLE" dusty or evolved star. Our selection criteria stipulate relative consistency in stellar type categorization across the three CMDs. Because some differences in categorization can result as a consequence of the different sensitivities afforded to the various wavelength regimes (e.g., CMD1 can better identify foreground stars, while CMD3 is better for classifying very dusty sources), such small inconsistencies will not disqualify a source from a "RELIABLE" label.

A source is considered a "RELIABLE" M-type star candidate when it is classified as an RSG or an O-rich AGB star in CMD1 and CMD2, and so long as it is not categorized as a dust-enshrouded source in CMD3. Of the M-type stars, RSGs are those which inhabit Region 2 in both CMD1 and CMD2, while O-rich AGB stars are those which inhabit Region 3 in both CMD1 and CMD2, or else is categorized as Region 3 in one of these two CMDs and as Region 2 in the other. Categorization within Region 3 in at least one of CMD1 or CMD2 favors a source to be an O-rich AGB star rather than an RSG. Previous study of the LMC employing CMDs equivalent to our CMD1 (Nikolaev & Weinberg 2000) and CMD2 (Blum et al. 2006) identified features blueward of the O-rich AGB star sequence, categorizing the relevant sources as RSGs. These classifications were then confirmed through spectroscopic cross-correlation. Boyer et al. (2011) extended this technique to the SMC to assess a distinction between RSGs and O-rich AGB stars, which was later revisited by Yang et al. (2018, 2019). With theoretical support from the modeling of Dell'Agli et al. (2015), we have adopted this prior proven technique for understanding the distinction between RSGs and O-rich AGB stars in CMDs applied to other galaxies.

Table 7
Categorization Region Combinations Amalgamated from the CMD Classifications for "RELIABLE" RSGs, O-rich AGB stars, C-rich AGB Stars, and YSOs

Type	CMD1 Region K versus $J-K$		CMD2 Region [3.6] versus $J-$ [3.6]		CMD3 Region [8.0] versus [3.6]–[8.0]
RSG:	2	&	2	&	NOT 5
O-rich AGB star:	2	&	3	&	NOT 5
	3	&	2	&	NOT 5
	3	&	3	&	NOT 5
C-rich AGB star:	4	&	4	&	NOT 5
	4	&	NOT 5	&	4
	NOT 5	&	4	&	4
YSO:	5	&	…	&	…
	…	&	5	&	…
	…	&	…	&	5

Note. Note that YSOs require the additional criterion that these sources fall within one of the seven star-forming regions demarcated in Figure 8.

In total, $n = 2342$ sources have been classified as "RELIABLE" M-type star candidates, with $n = 1292$ of these being designated as RSGs and $n = 1050$ as O-rich AGB stars. "RELIABLE" C-type star candidates are those which are categorized as C-rich in at least two of the three diagnostic CMDs, and are additionally never categorized as dust-enshrouded in any of the three CMDs. There are $n = 560$ sources classified as "RELIABLE" C-type star candidates. A source is considered a "RELIABLE" YSO candidate only when it is categorized as a dust-enshrouded object in each of the three CMDs. In addition, because YSOs are definitively restricted to regions of recent star formation, which are found in clusters, we have included a secondary requirement that a YSO is categorized as "RELIABLE" only if it is found within one of seven star formation regions where the number density of YSO candidate sources is highest (e.g., Jones et al. 2019). This yields a final total of "RELIABLE" YSO candidates of $n = 277$. A spatial distribution plot of all "RELIABLE" sources is presented as Figure 8, while classification criteria are presented in Table 7.

Other types of sources, including background galaxies and foreground/MS stars, were similarly classified based on their categorizations from the three diagnostic CMDs. Because our methods are not optimized for such sources, we refrain from detailed explanations of these objects' classifications. Rather, we note that such sources were identified outside of the RSG, AGB star, and YSO candidate color cuts. Finally, sources that are determined to be reliably unclassifiable are those which do not receive categorization into any of the possible stellar types in any of the diagnostic CMDs.

A further $n = 260$ (0.8%) objects have been classified as "CANDIDATE" sources, indicating that the confidence level in

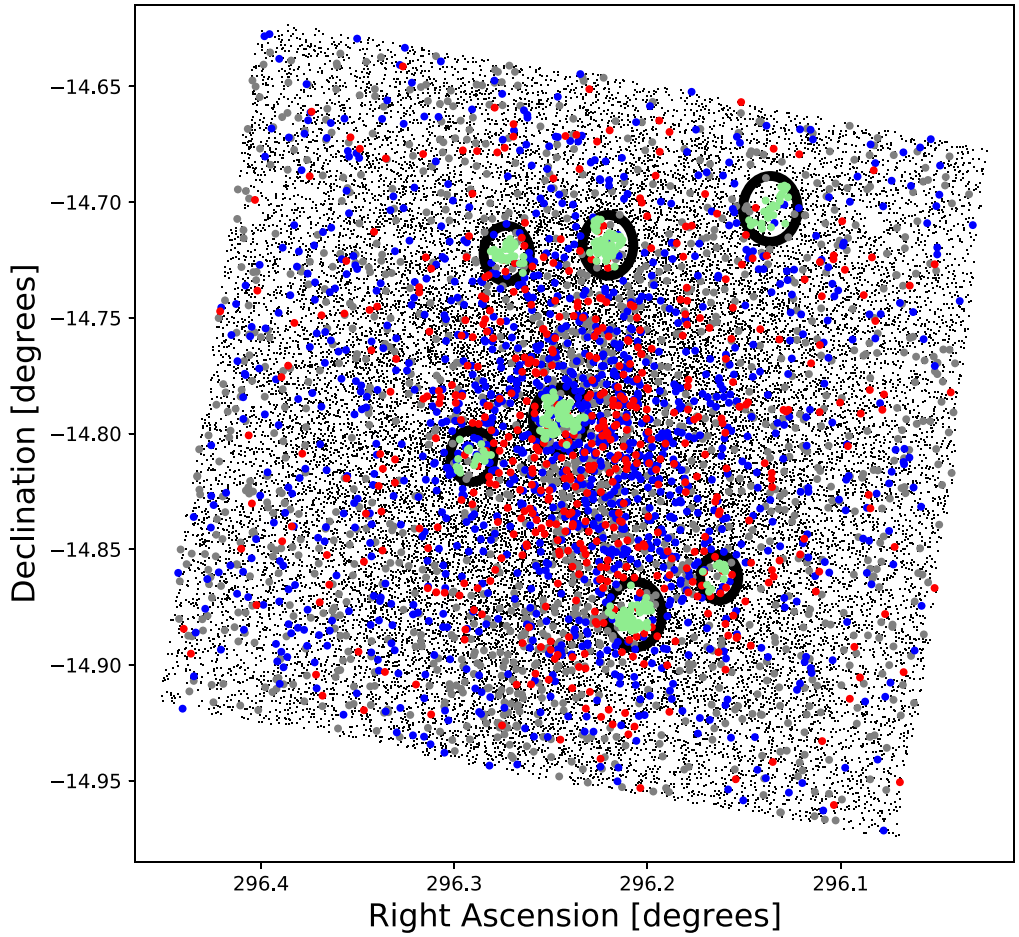

Figure 8. Spatial distribution plot combining the locations of "RELIABLE" RSGs (gray dots), O-rich AGB stars (blue dots), C-rich AGB stars (red dots), and YSOs (green dots) over all sources included in the master source catalog (black points). The black rings signify the location of the star-forming regions used in the source classification algorithm detailed in Section 3.3. Prominent and well-known star-forming regions are discernible along the top and bottom of the structure of NGC 6822. Recent work, presented both here and in Jones et al. (2019), reveals a young, embedded star-forming region located centrally within the N−S bar. This cluster, known as Spitzer I, is located at R.A. = $19^{h}44^{m}58\overset{s}{.}97$, decl. = $-14^{d}47^{m}37\overset{s}{.}39$ and presents an exciting new object for future study.

their combined stellar type categorizations is lower than for the "RELIABLE" targets. This is typically due to more pronounced inconsistencies in classification defined across the three CMDs than was allowable for the "RELIABLE" targets, while retaining photometric characteristics consistent with a particular stellar type. While very few such "CANDIDATE" sources populate our catalog as compared to "RELIABLE" sources, we felt their inclusion was warranted as a preliminary means of classification, with expectation for more sophisticated techniques applied later. The combination of diagnostic CMD categorizations for "CANDIDATE" sources follow similar structure to those of "RELIABLE" sources. These selection criteria are summarized in Table 8. In total, our catalog of "CANDIDATE" objects includes $n = 65$ RSGs, $n = 59$ O-rich AGB stars, $n = 27$ C-rich AGB stars, and $n = 109$ extremely dusty objects. We note that a source that would qualify as a "RELIABLE" YSO but lies outside of the star-forming regions is thus classified as a "CANDIDATE" C-type star. These dust-enshrouded sources, most predominantly selected from the longer wavelength color cuts of CMD3, include both YSOs and perhaps a rare class of the dustiest extreme AGB stars ("x-AGB" stars; see Blum et al. 2006; Boyer et al. 2011, 2015a). These x-AGB stars have been found to produce an extremely large proportion of dust for their small numbers in metal-poor, star-forming environments.

Finally, CMD categorization region combinations for background galaxies ($n = 13{,}765$, 44.8%) and foreground/MS stars ($n = 1931$, 6.3%) are summarized in Table 9, totaling 15,687 sources (51.1%). The remaining $n = 1660$ (5.4%) of sources are left as "CLASSLESS." These objects' photometric properties provided no obvious identity based on categorical consistency within the three CMDs and were therefore left unclassified. Comprising a relatively small minority of the overall sample, we expect future categorization with more sophisticated identification techniques to shed light on these sources. The demographic results of the "RELIABLE" and "CANDIDATE" catalogs are summarized in Table 10, along with all "OTHER" sources. Source classification demographics are illustrated as pie charts for both the entire joined catalog and only "RELIABLE" dusty and evolved stars in Figure 9.

3.4. Removing Contaminants

Contamination of the various source catalogs developed through this study has been somewhat mitigated via our color-cut specifications; however, some number of inadvertent contaminants must be expected. Near- and mid-IR colors of red supergiant stars (RSGs) are similar to those on the AGB, and at the distance of NGC 6822, unresolved background galaxies, including star-forming galaxies and active galactic

Table 8
Categorization Region Combinations Amalgamated from the CMD Classifications for "CANDIDATE" O-rich AGB stars, C-rich AGB Stars, and Extremely Dusty Objects

Type	CMD1 Region K versus $J-K$		CMD2 Region [3.6] versus $J-$ [3.6]		CMD3 Region [8.0] versus [3.6]–[8.0]
RSG:	2	&	1	&	1
O-rich AGB star:	3	&	4	&	2
C-rich AGB star:	4	&	5	&	4
extremely dusty:	5	&	5	&	4

Table 9
Categorization Region Combinations Amalgamated from the CMD Classifications for Background Galaxies and Foreground/MS Stars

Type	CMD1 Region K versus $J-K$		CMD2 Region [3.6] versus $J-$ [3.6]		CMD3 Region [8.0] versus [3.6]–[8.0]
Background galaxy:	1	&	1	&	6
	1	&	…	&	6
	…	&	1	&	6
	…	&	…	&	6
Foreground/ MS star:	1	&	1	&	1
	1	&	1	&	2
	1	&	1	&	5
	1	&	1	&	…
	1	&	2	&	2
	…	&	…	&	2
	1	&	…	&	1
	…	&	1	&	1
	…	&	…	&	1

Table 10
Demographics of the "RELIABLE" and "CANDIDATE" Stellar Source Catalogs, Plus All "OTHER" Source Types (Including Background Galaxies, Foreground/MS Stars, Unclassifiable, and Unclassed)

Catalog	Stellar Type	Number of Sources
"RELIABLE"	RSGs	1292
	O-rich AGB	1050
	C-rich AGB	560
	YSOs	277
"CANDIDATE"	RSGs	65
	O-rich AGB	59
	C-rich AGB	27
	Extremely Dusty	109
"OTHER"	Background Galaxies	13,765
	Foreground/MS Stars	1931
	Unclassifiable	9950
	Classless	1660

nuclei, have colors that significantly overlap those of dusty sources and YSOs (Jones et al. 2019). Due to the lower luminosity of the populations, magnitude-based cutoffs used effectively at selecting AGB stars and YSOs in the Magellanic Clouds are less efficient in systems at greater distances, such as NGC 6822.

Estimating conservative upper limits for source contamination, we assume a random and homogeneous distribution of background galaxies and foreground stars across our field of interest. We have adopted an area of 10.80 arcmin^2 on the outskirts of the galaxy, away from known star formation regions, to estimate the approximate level of contamination in our source cuts, similar to the method implemented by Jones et al. (2019). With 476 point sources in this off-target box identified from the master catalog, this region has a total point-source density of 44.07 sources per arcmin^2. We calculate the maximum contamination percentage for each of the RSG, O-rich AGB star, C-rich AGB star, and dust-enshrouded source candidates (including YSOs) for each of the three diagnostic CMDs (where appropriate), as well as our "RELIABLE" source lists. Results are summarized in Table 11. From this analysis, we estimate a maximum contamination percentage for our "RELIABLE" source lists to be 52.93% for RSGs, 29.52% for O-rich AGB stars, and 20.76% for C-rich AGB stars. Because our selection criteria for "RELIABLE" YSOs require inclusion within star-forming regions (see Figure 8), this off-target contamination study necessarily yields zero erroneous sources. CMDs of the master catalog sources contained within the off-target comparison region are presented as Figure 10. Overplotted are objects from the "RELIABLE" catalogs, including RSGs and both O- and C-rich AGB stars. Note that because no YSOs appear in this off-target comparison region, none appear in these CMDs.

In addition to a statistical investigation of contamination sources, we queried the SIMBAD and VizieR Astronomical Databases using the CDS X-Match Service[8] for associations of our RSG, AGB star, and YSO candidates with other known astronomical objects. Within a 2″ radius, 646 RSGs, 840 O-rich AGB stars, 530 C-rich AGB stars, and 148 YSOs were matched to sources with literature classifications. These mostly comprise AGB star candidates identified using optical or near-IR colors (Letarte et al. 2002; Kang et al. 2006; Sibbons et al. 2012; Whitelock et al. 2013). In addition, there are matched classifications indicative of youth, e.g., Hα-emitting objects (Massey et al. 2007), CO-bright clumps (Schruba et al. 2017), and compact H II regions (Hernández-Martínez & Peña 2009), and presence within a star-forming region (Melena et al. 2009). Finally, a handful sources have been matched to spectroscopically confirmed red giant stars (Kirby et al. 2017).

Of the RSGs, 3 have been matched to red giants, 4 have been matched to Hα emission-line stars, and 23 to star-forming regions. Twenty-three sources had conflicting classifications (all but three of which are classified as both star-forming regions and AGB stars). For O-rich AGB stars, 2 have been matched to red giants, 4 have been matched to Hα emission-line stars, 15 to star-forming regions, and 1 to a CO-bright clump. Conflicting classifications occurred for 21 sources. C-rich AGB stars match to three red giants, five Hα emission-line stars, nine star-forming regions, and two CO-bright

[8] http://cdsxmatch.u-strasbg.fr/#tab=xmatch

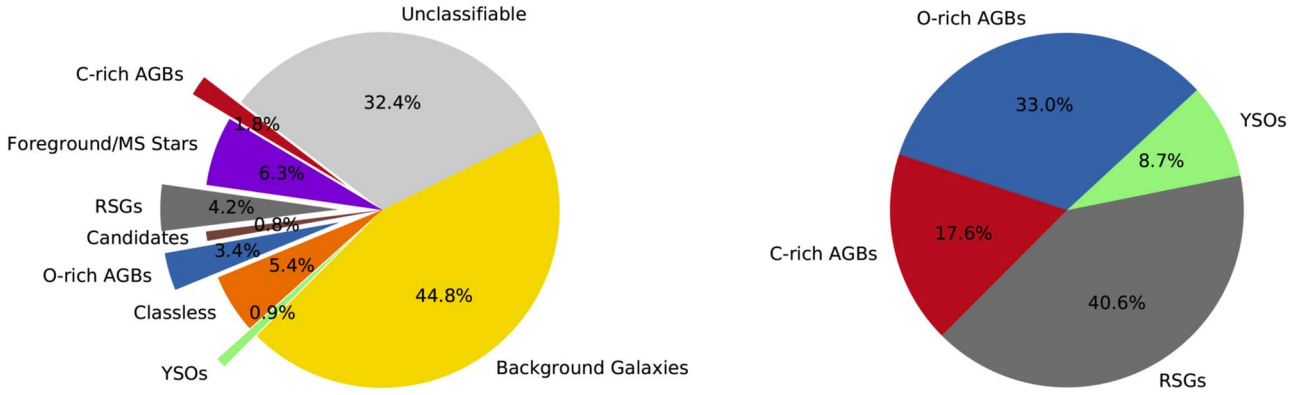

Figure 9. Pie charts illustrating the classification demographics of the entire joined catalog (left) and of only the "RELIABLE" dusty and evolved stars (right). For the "RELIABLE" catalog, RSGs (gray) number 1292 sources, O-rich AGB stars (blue) number 1050 sources, C-rich AGB stars (red) number 560 sources, and YSOs (green) number 277 sources. All other source types include "CANDIDATE" objects (n = 260), background galaxies (n = 13,765), foreground/MS stars (n = 1931), unclassifiable (n = 9950), and classless (n = 1660).

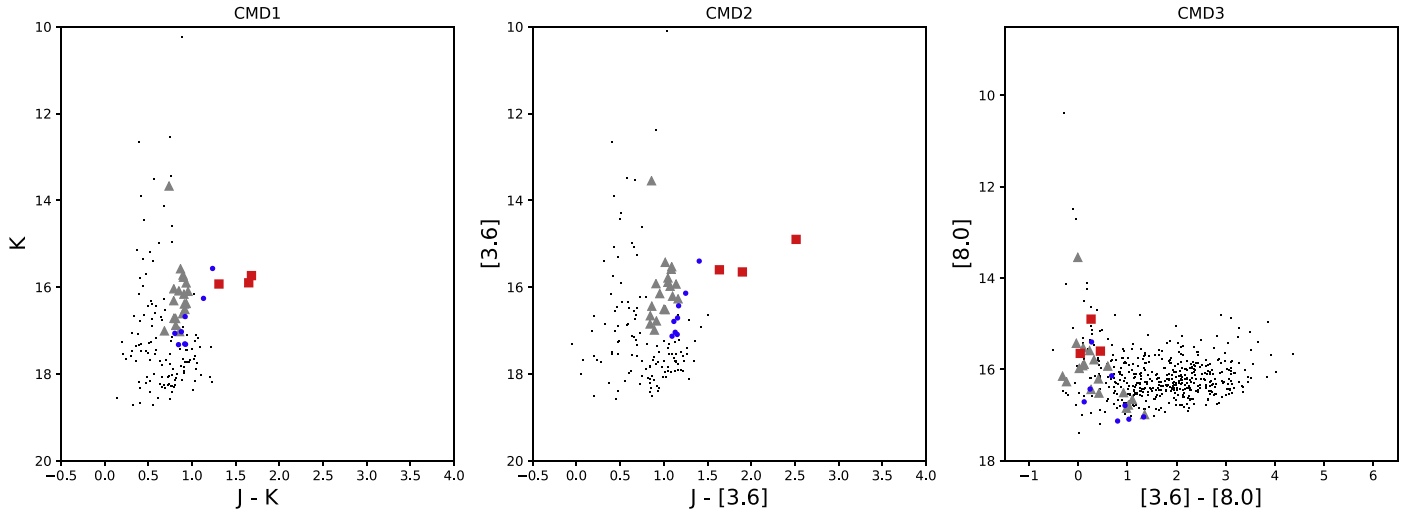

Figure 10. Diagnostic CMDs of sources from the master catalog contained within the off-target comparison box used to compute contamination (gray points; see Table 11). Overplotted are sources from our "RELIABLE" catalogs, including RSGs (gray triangles), O-rich AGB stars (blue dots), and C-rich AGB stars (red squares). YSOs are not included here as none appear in the off-target comparison box.

Table 11
Contamination Estimates from Off-target Comparison Region

CMD Catalog	Source Type	Number of Sources in Box	Contaminant Sources [arcmin^{-2}]	Average Number of Contaminants in Entire FoV	Number of Color--Selected Sources in Entire FoV	Maximum Contamination Percentage [%]
K versus $J-K$	RSGs	40	3.70	1550.00	2075	74.70
K versus $J-K$	O-rich AGB	7	0.65	271.25	1002	27.07
K versus $J-K$	C-rich AGB	7	0.65	271.25	907	29.91
K versus $J-K$	Dust-enshrouded	0	0.00	0.00	144	0.00
[3.6] versus $J-$ [3.6]	RSGs	19	1.76	736.25	1571	46.87
[3.6] versus $J-$ [3.6]	O-rich AGB	15	1.39	581.25	1545	37.62
[3.6] versus $J-$ [3.6]	C-rich AGB	3	0.28	1916.25	713	16.30
[3.6] versus $J-$ [3.6]	Dust-enshrouded	0	0.00	0.00	230	0.00
[8.0] versus [3.6] − [8.0]	M-type (all)	3	0.28	116.25	674	17.25
[8.0] versus [3.6] − [8.0]	C-rich AGB	33	3.06	1278.75	2949	43.36
[8.0] versus [3.6] − [8.0]	Dust-enshrouded	3	0.28	116.25	630	18.45
"RELIABLE"	RSGs	19	1.76	736.25	1391	52.93
"RELIABLE"	O-rich AGB	8	0.74	310.00	1050	29.52
"RELIABLE"	C-rich AGB	3	0.28	116.25	560	20.76
"RELIABLE"	YSOs	0	0.00	0.00	277	0.00

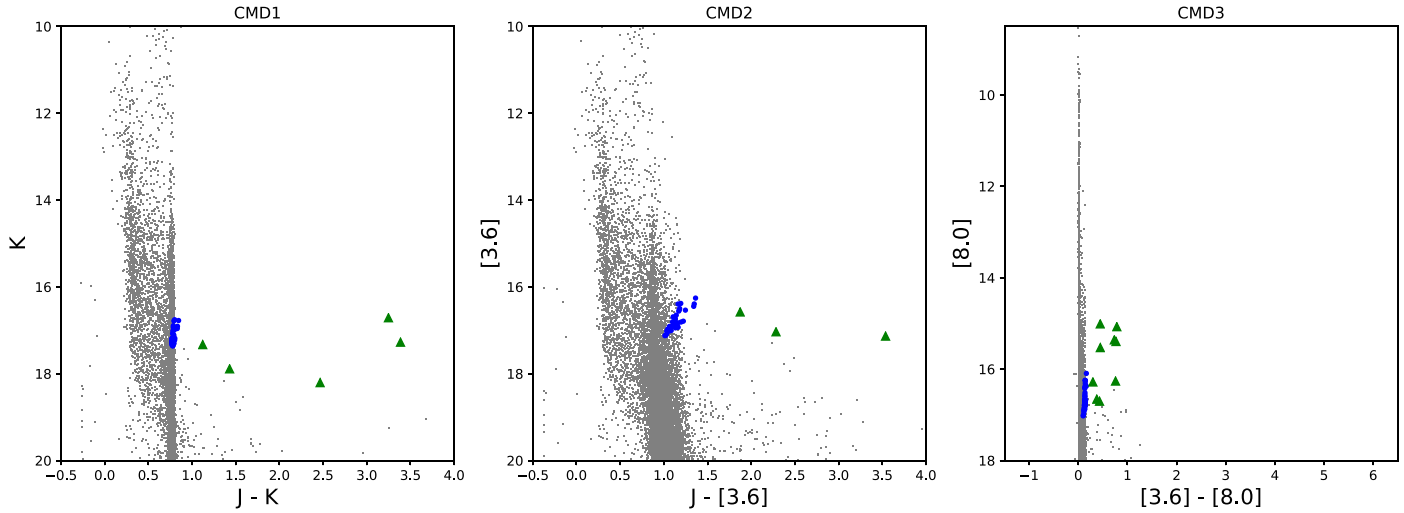

Figure 11. Diagnostic CMDs of sources from the TRILEGAL Galaxy model, processed through the same color-cut classification criteria as are applied to the "RELIABLE" sources from our master catalog. Gray points represent all foreground sources from TRILEGAL. Model O-rich AGB stars are shown as blue dots, while YSOs are shown as green triangles. Zero C-rich AGB stars were selected from the modeled data and so do not appear in these plots.

clumps. Seventeen sources presented conflicting classifications. Finally, 1 YSO was matched to a red giant (likely the result of a chance superposition of one optically bright and one IR-bright source in the crowded field), 7 matched to H II regions, 2 to planetary nebulae (PNe), 20 to Hα emission-line stars, 10 to star-forming regions, 10 to Hα emission regions from UV data, and 80 to CO-bright clumps. We note that mid-IR Spitzer colors for YSOs and PNe are indistinguishable and require spectral disentanglement and are thus potentially significant sources of contamination (Jones et al. 2017b). There were 31 instances of conflicting classifications.

Finally, we employed the TRILEGAL service[9] to better understand foreground sources of contamination. This tridimensional model of the Galaxy (Girardi et al. 2012) is used to populate the field of view to NGC 6822 with artificial foreground stars, which are then run through the same color-cut classification criteria as are applied to our master catalog sources. Because completeness of the data is not well defined at blue wavelengths, this technique was implemented to grasp the likelihood of foreground contamination by O- and C-rich AGB stars and YSOs. CMDs of all sources obtained from the TRILEGAL Galaxy model are presented as Figure 11. This data was subsequently processed through the same color-cut classification criteria as applied to the "RELIABLE" dusty and evolved star catalogs, producing artificial contaminants which have been overplotted. In total, we found 41 simulated O-rich AGB star contaminants, 0 such C-rich AGB stars, and 9 YSOs.

4. Discussion

With the categorizations of the stellar types established in Section 3.3, we now examine the spatial distribution of dusty and evolved stars in NGC 6822 and compare these results with other studies available in the literature. A plot of all points in R.A. and decl. space from our master catalog effectively produces a synthetic map of the galaxy. A comparison with the image of NGC 6822 (Figure 1) reveals that such a spatial distribution plot features the same main structural components, including the central bar (running N–S) within which the density of the individual sources is highest. We present the spatial distributions of the evolved star populations from our "RELIABLE" catalogs as Figure 12. The AGB star candidates (O rich, upper left; C rich, upper right) appear correlated with the extent and structure of the galaxy. These points are situated primarily within the central N–S bar of NGC 6822 and therefore appear to have been successfully selected by the color-cut classification technique to be physically associated with the galaxy itself. The RSG candidates (lower left) demonstrate a strong clustering along the central bar as well, though with a higher number of points distributed homogeneously across the field of view. As discussed in Section 3.4, the RSG color cut is strongly influenced by contamination from foreground sources, which may account for this effect. Finally, the selection criteria for YSO candidates (lower right) necessitates that they are confined to within the seven major star formation regions as defined in Section 3.3. These include the well-known Hubble star-forming regions (i.e., Hubble X, Hubble V, and Hubble I and III along the north side, and Hubble IV on the south side of NGC 6822), as well as three newly identified, young, embedded clusters dubbed Spitzer I, II, and III, which were introduced in Jones et al. (2019) and discussed further in Section 4.2.

4.1. Calculations of Stellar Metallicity

With a census of "RELIABLE" O- and C-rich AGB star candidates determined through our color-cut classifications, we can investigate the stellar metallicity characteristics of this galaxy. The ratio of the number of C-rich (C-type) to O-rich (M-type) AGB stars can be used as a gauge of the star formation environment. For a lower initial ambient metallicity, fewer dredge-up events are necessary to form a C-rich atmosphere, and thus a higher measured value of the overall C/M ratio is expected compared to a solar-metallicity environment (Groenewegen 2006 and references therein; Sibbons et al. 2012; Boyer et al. 2017; Boyer 2019). In addition, a lower metallicity environment will push the AGB evolutionary track toward higher temperatures. This has the further result of reducing the numbers of M-type stars while simultaneously increasing the number of K spectral type RGB stars (Iben & Renzini 1983; Marigo et al. 1999; Sibbons et al. 2012). By the relation of Battinelli & Demers (2005) and refined by

[9] http://stev.oapd.inaf.it/cgi-bin/trilegal

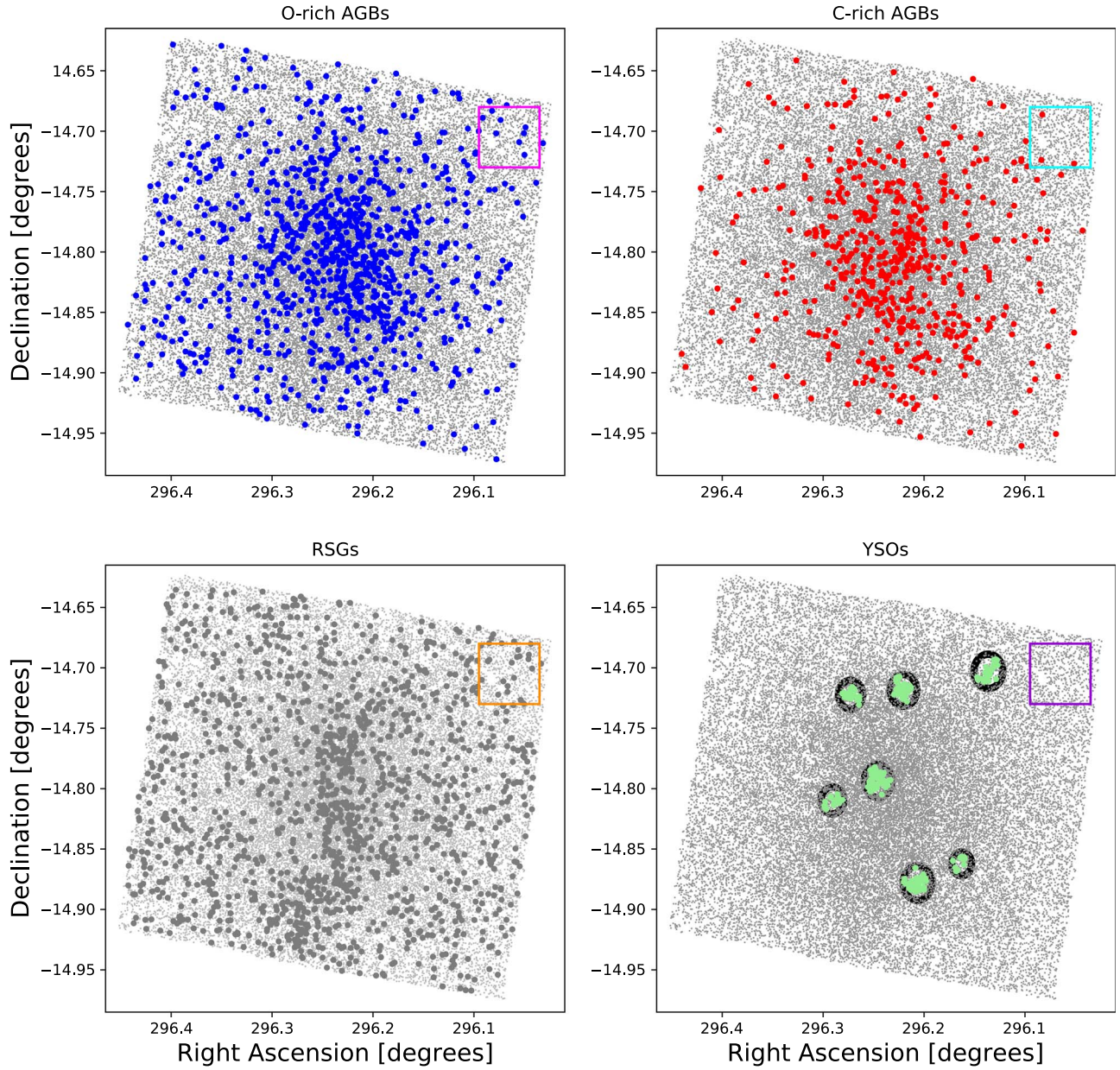

Figure 12. Spatial distribution plots of O-rich AGB star (blue points; upper left), C-rich AGB star (red points; upper right), RSG (gray points; lower left), and YSO candidates (green points within black rings; *lower right*). Colored points are overplotted on all sources in the NGC 6822 master catalog (gray dots). The region used to determine contamination percentages (presented in Table 11) is included in the top right of each plot as a colored box.

Cioni (2009),

$$[\mathrm{Fe/H}] = -1.39 \pm 0.06 - 0.47 \pm 0.10 \times \log(\mathrm{C/M}). \quad (1)$$

The C/M ratio for NGC 6822, computed over the entire field of view for our study, is 0.533 ± 0.028. We therefore find a metallicity for NGC 6822 of $[\mathrm{Fe/H}] = -1.262 \pm 0.098$. Corrected for maximum source contamination (see Table 11), the C/M ratio becomes 0.599 ± 0.036, which gives a metallicity $[\mathrm{Fe/H}] = -1.286 \pm 0.095$. The study of Sibbons et al. (2012) report a C/M ratio of 0.23 ± 0.01 over their full-observed area, which produces a metallicity estimate of $[\mathrm{Fe/H}] = -1.14 \pm 0.08$ utilizing the same Cioni (2009) relation. Within 4 kpc of the center, however, they report a C/M ratio of 0.48 ± 0.02, equivalent to $[\mathrm{Fe/H}] = -1.24 \pm 0.07$. For a distance to NGC 6822 of 490 kpc, a radius 4 kpc from the galaxy center is equivalent to $28\farcm06$, which is larger than the field of view of our study as dictated by the extent of the Spitzer data. This second metallicity from Sibbons et al. (2012) is therefore a much more appropriate comparison to our own reported value, which agrees within the respective errors.

In addition, we have investigated the AGB stars in NGC 6822 for possible structure in the metallicity distribution of this galaxy. First, by segregating the AGB stars along the central N−S bar, we investigate the variability of metallicity across the galactic axis of rotation. We adopt the coordinates for the center of NGC 6822 from Sibbons et al. (2012) as R.A.$=19^{\mathrm{h}}44^{\mathrm{m}}56^{\mathrm{s}}$, decl. $= -14^{\mathrm{d}}48^{\mathrm{m}}06^{\mathrm{s}}$, and the angle of the axis rotation of 330° adopted from McConnachie (2012). On the left side of NGC 6822, we find a C/M ratio of 0.507 ± 0.038, which corresponds by Equation (1) to $[\mathrm{Fe/H}] = -1.251 \pm 0.105$. On the right side of the galaxy, we find a C/M ratio of 0.561 ± 0.041, giving a metallicity of $[\mathrm{Fe/H}] = -1.272 \pm 0.100$. When corrected for

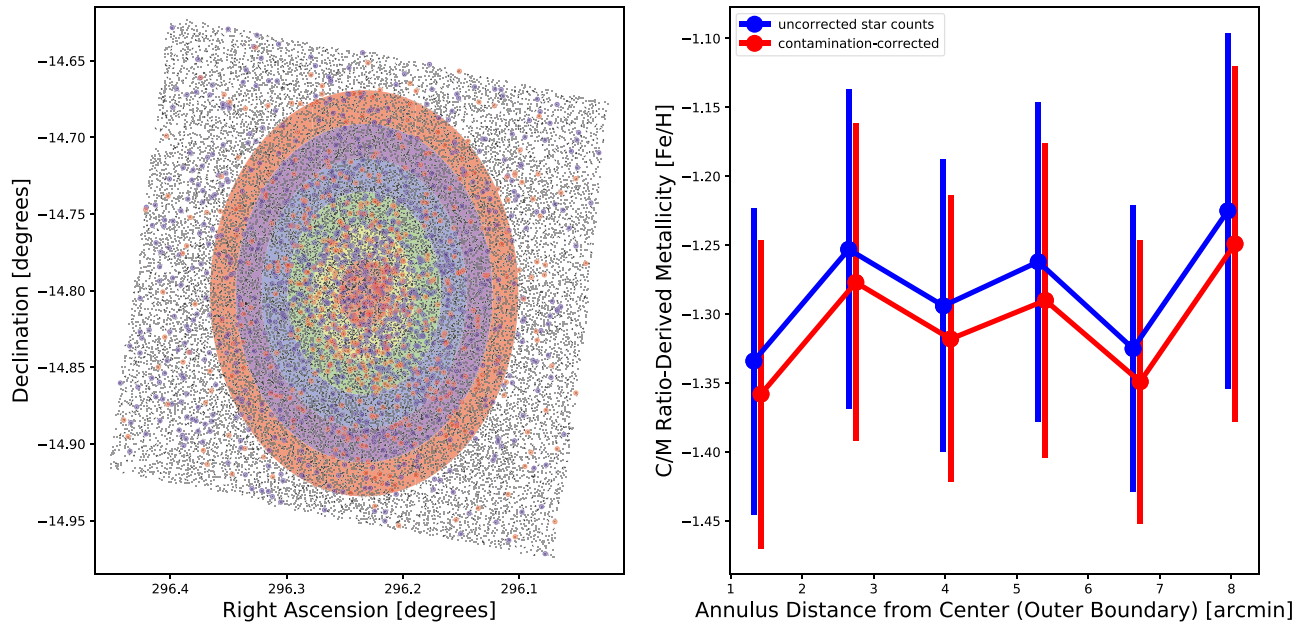

Figure 13. Metallicity analysis via C/M ratio in NGC 6822 along circular annuli originating at the center and increasing outwards (left). O-rich AGB stars are represented as blue dots, while C-rich AGB stars are represented as red dots. These overplot all sources from the master catalog, shown as gray dots. Each annulus is $1\farcm325$ in width, corresponding to the quarter-light (red ellipse), half-light (yellow ring), three-quarter-light (green ring), full-light (blue ring), one-and-one-quarter-light (violet ring), and one-and-one-half-light (orange ring) radii. The stellar metallicity [Fe/H] computed from the C/M ratio relation of Cioni (2009) is plotted as a function of annulus distance from the galaxy center (right; see Table 12). Values from uncorrected star counts are presented in blue, while contamination-corrected values are presented in red (with a small arbitrary x-axis value offset to avoid overlap). We find an increase in metallicity with increasing distance. The rate of increase is very slight, however, and all values of metallicity agree within their respective errors, therefore giving only a tenuous suggestion of a radial metallicity gradient.

Table 12
C/M Ratio and [Fe/H] Values for Concentric Radial Rings Originating from the Center of NGC 6822

Inner Ring Boundary Distance from Center [arcmin]	Outer Ring Boundary Distance from Center [arcmin]	C/M (uncorrected star counts)	[Fe/H] (uncorrected star counts)	C/M (contamination -corrected)	[Fe/H] (contamination -corrected)
0.000	1.325	0.761 ± 0.141	-1.334 ± 0.111	0.856 ± 0.183	-1.358 ± 0.112
1.325	2.650	0.511 ± 0.065	-1.253 ± 0.116	0.575 ± 0.084	-1.277 ± 0.115
2.650	3.975	0.625 ± 0.076	-1.294 ± 0.106	0.703 ± 0.098	-1.318 ± 0.104
3.975	5.300	0.544 ± 0.073	-1.262 ± 0.116	0.612 ± 0.094	-1.290 ± 0.114
5.300	6.625	0.726 ± 0.104	-1.325 ± 0.104	0.817 ± 0.134	-1.349 ± 0.103
6.625	7.950	0.446 ± 0.073	-1.225 ± 0.129	0.502 ± 0.094	-1.249 ± 0.129

maximum source contamination, the left-side C/M ratio becomes 0.570 ± 0.049, corresponding to a metallicity of [Fe/H] $= -1.275 \pm 0.102$. The contamination-corrected values for the right side are a C/M ratio of 0.631 ± 0.053, which gives a metallicity [Fe/H] $= -1.296 \pm 0.097$. The measured stellar abundances of these two halves of NGC 6822 fall neatly on either side of the overall metallicity of [Fe/H] $= -1.262 \pm 0.098$ ([Fe/H] $= -1.286 \pm 0.095$ when corrected for contamination) discussed earlier; however, the magnitude of the difference is minuscule in comparison with the respective errors. We therefore conclude that the rotation of NGC 6822 has no impact on the measured stellar metallicity of the system.

Second, we have isolated the C- and M-type AGB star populations in six concentric rings of width equal to the quarter-light radius ($1\farcm325$; ∼0.189 kpc), initiating from the center of the galaxy. Within these rings, we compute the C/M ratio and the associated value of [Fe/H] out to a distance of $7\farcm95$ (∼1.133 kpc), equivalent to the one-and-one-half-light radius. We find a minimum value of [Fe/H] $= -1.334 \pm 0.111$ in the most central annulus, with metallicities increasing with expanding radius to a maximum of [Fe/H] $= -1.225 \pm 0.129$ in the outermost ring ([Fe/H] $= -1.358 \pm 0.112$ to -1.249 ± 0.129 when contamination corrected). These results are illustrated in Figure 13 and summarized in Table 12. The rate of increase we find for NGC 6822 is quite minimal, however, and all values of metallicity agree within their respective errors, therefore giving only a very slight suggestion of a radial metallicity gradient. We therefore do not suggest the reality of a radial metallicity gradient in NGC 6822.

Overall, these values of the stellar metallicity depend on the implicit assumption that all C- and O-rich AGB star candidates from our "RELIABLE" catalog are actually AGB stars. Computations utilizing maximum contamination percentage corrected values are the only avenue in this analysis. While our classification methodology requires candidacy from multiple CMDs to be marked as "RELIABLE" for the sake of redundancy, the presence of contaminant RGBs in our M-type star catalog cannot be ignored. Our C/M ratios and [Fe/H] values must therefore be considered as lower limits. The true nature of these sources requires more sophisticated analysis than color-cut segregations can provide. Future studies employing spectral energy distribution (SED) fitting promise to refine this value even further with higher-confidence identifications of the relevant stellar populations.

4.2. The Young, Embedded Star-forming Regions Spitzer I, Spitzer II, and Spitzer III

The bright, well-known star-forming complexes of NGC 6822 (e.g., Hubble X, Hubble V, and Hubble I and III situated along the north side, and Hubble IV situated on the south side of the galaxy), distinguished by optically conspicuous Hα emission (see Figure 1), have been studied extensively across several wavelength regimes. Hubble (1925) first presented optical plates of NGC 6822, identifying conspicuous star-forming regions. Hα fluxes of the two brightest H II regions, Hubble V and Hubble X, were obtained by Kennicutt (1979), which were later observed with HST by O'Dell et al. (1999). Hodge et al. (1988) compiled an atlas of H II regions via optical survey, while Hodge et al. (1989) provided an Hα luminosity function and H II region size distribution. Gallagher et al. (1991) and Israel et al. (1996) studied the star-forming regions in the far-IR. CO emission was studied to trace molecular gas by Israel et al. (2003) and later, on a larger scale, by Schruba et al. (2017). Cannon et al. (2006) presented Spitzer imaging of emission regions in NGC 6822 to study the nature of IR, Hα, H I, and radio continuum emission. Gouliermis et al. (2010) employed optical photometry and stellar density maps to show the hierarchical stellar structure in the galaxy, linking some stellar concentrations with IR-bright complexes identified with Spitzer imaging from Cannon et al. (2006). Finally, several studies have used the massive H II regions of NGC 6822 as specimens of extragalactic star formation, employing Spitzer spectroscopy to study photodissociation, fine-structure lines, and abundance ratios (e.g., Lee et al. 2005; Hunter & Kaufman 2007; Rubin et al. 2016).

The spatial distribution of "RELIABLE" YSO candidates is illustrated in the lower right of Figure 12. Sources are tightly clustered in compact regions consistent with the well-known star-forming regions of NGC 6822. In addition to these, we have identified comparable numbers of dusty sources grouped in other tight clusters. Located coincident with the central N−S bar, these collections of red-excess objects appear to be massive, embedded regions of star formation that have been otherwise hidden from previous optical surveys. Only via concentrated effort with near- and mid-IR photometry are these obscured clusters of YSO candidates revealed. The most central star-forming region, dubbed Spitzer I by Jones et al. (2019), is located at R.A. $= 19^{h}44^{m}58\overset{s}{.}97$, decl. $= -14^{d}47^{m}37\overset{s}{.}39$ and is home to 80 of the "RELIABLE" YSOs identified in this study. Cannon et al. (2006) categorized this region as the infrared source "NGC 6822 11," cross-listed as Hubble VI and VII, while Gratier et al. (2010) studied the molecular cloud complexes of this region in CO. Immediately adjacent to Spitzer I is the smaller Spitzer II, located at R.A. $= 19^{h}45^{m}09\overset{s}{.}80$, decl. $= -14^{d}48^{m}34\overset{s}{.}77$, and within which we have found 18 YSOs. Finally, next to Hubble IV in the south of NGC 6822 is Spitzer III, located at R.A. $= 19^{h}44^{m}39\overset{s}{.}08$, decl. $= -14^{d}51^{m}44\overset{s}{.}12$, and which contains 14 YSOs.

The high concentration of YSO candidates within these star-forming regions, along with the strong likelihood of source confusion due to crowding and resolution effects, suggests a larger number of individual YSOs than our selection criteria are capable of singling out. The observational signature of Spitzer I may in fact indicate the presence of a proto-super-star cluster (SSC; $M_{*} \gtrsim 10^{5}\ M_{\odot}$). SSCs are representative of a star formation mode where stellar surface densities exceed that of H II regions and OB associations by orders of magnitude (Nayak et al. 2019) and may be early-universe analogs to modern-day globular clusters. The most well-known SSC is the cluster R136, which resides within the massive LMC star-forming region 30 Doradus. A parallel star-forming complex known as N79, identified to possess Hα-emitting sources first by Henize (1956), occupies space symmetrically across the bar of the LMC, discernible in the distribution of H I gas (see Figure 1 of Ochsendorf et al. 2017). Within the southernmost of three giant molecular clouds in N79 is the object H72.97−69.39, originally thought to be the most luminous YSO in the entire LMC (Seale et al. 2014), but recently identified as a proto-SSC (Ochsendorf et al. 2017; Nayak et al. 2019).

In contrast to the optically luminous and conspicuous 30 Doradus, the N79 region is weak in optical star formation tracers such as Hα emission. Ochsendorf et al. (2017) have found N79 to be extremely active, however, hosting a densely packed population of YSOs. Similarly, while roughly equivalent in physical size to Hubble V, the brightest H II region in NGC 6822 (radius ≈120 pc), our identification of 80 YSOs associated with Spitzer I is ∼50% more than were found in Hubble V ($n = 55$), demonstrating a high density of young stars. Spitzer I is rich in molecular gas (inferred from 8 μm emission; Sandstrom et al. 2012) and is probably the youngest star-forming region in NGC 6822 (Jones et al. 2019). Furthermore, analyses of star formation tracers reveal a higher level of IR flux as compared to UV or Hα, providing a strong indication that the SFR is expected to increase. Similarly to the LMC object H72.97−69.39 in N79, Spitzer I has yet to reach its peak level of star formation activity and may potentially become an SSC. While the question of exactly *how* SSCs form remains a mystery, future detailed studies of H72.97−69.39 and Spitzer I may shed light on this extreme star formation phenomenon.

The recent work of Jones et al. (2019) employed the joined master catalog developed in this study to specifically characterize the YSO population of NGC 6822. Utilizing an independent set of color-cut criteria, Jones et al. (2019) have identified 90 YSOs within the region of space affiliated with Spitzer I. Their classification system further employed SED modeling, finding the Spitzer I YSOs exhibiting properties characteristic of the earliest stages of formation. It is rich in molecular gas and has substantial emission in 8 μm as well as some emission in 24 μm, but is faint in Hα and UV. Combined with a large H I mass, the large population of high-confidence YSO detections strongly indicate that this star-forming region is young and very embedded, exhibiting the highest SFR known in NGC 6822 (Jones et al. 2019). Future observations with JWST promise to characterize this potential proto-SSC with exceptional detail.

5. Summary

In this study, we have combined near- and mid-IR photometric data from Sibbons et al. (2012) and Khan et al. (2015) of the nearby, metal-poor dwarf star-forming galaxy NGC 6822 to produce a catalog useful for characterization of dusty and evolved stars. Through implementation of KDE local minima analyses, including the Monte Carlo method KDE (or "MCKDE") technique used to define the TRGB, we have produced color cuts to categorize sources into several stellar type categories, including RSGs, O-rich AGB star candidates, C-rich AGB star candidates, and dust-enshrouded sources (including YSOs). These color-cut classifications were developed for three diagnostic CMDs, which span a wide range in wavelength space afforded by the available

data, and include K versus $J-K$ (CMD1), [3.6] versus J—[3.6] (CMD2), and [8.0] versus [3.6]—[8.0] (CMD3).

From these KDE-derived color-cut categorizations, overall source type classifications were established to produce "RELIABLE" and "CANDIDATE" catalogs. From a catalog with $N = 30{,}745$ total sources, $n = 3179$ have been classified as "RELIABLE" dusty and evolved stars (10.3% of the total catalog), while $n = 260$ have been classified as "CANDIDATE" (0.8% of the total catalog). Of these "RELIABLE" sources, $n = 1292$ are categorized as RSGs, $n = 1050$ are categorized as O-rich AGB stars, $n = 560$ are categorized as C-rich AGB stars, and $n = 277$ are categorized as YSOs. The small number of "CANDIDATE" sources include $n = 65$ RSGs, $n = 59$ O-rich AGB stars, $n = 27$ C-rich AGB stars, and $n = 109$ dust-enshrouded sources (which may include AGB stars or YSOs). The combined CMD color-cut categorizations of these objects are more ambiguous than for our "RELIABLE" object classifications. We categorize the majority of the remaining sources as either background galaxies ($n = 13{,}765$), foreground and MS stars ($n = 1931$), or, because they do not fall into type categorizations in any of the three diagnostic CMDs and/or possess only upper limits to their photometric uncertainty values, are considered unclassifiable ($n = 9950$). Finally, the remaining $n = 1660$ sources do not present an obvious type from our analysis and are therefore considered "CLASSLESS."

The spatial distribution of the "RELIABLE" evolved stars shows strong coincidence with the central N−S bar of NGC 6822 in the case of O- and C-rich AGB star candidates. Employing the relation of Cioni (2009), we determine a stellar metallicity of NGC 6822 of $[\mathrm{Fe/H}] = -1.286 \pm 0.095$ as defined by the ratio of C- to M-type AGB stars. This value is consistent with other studies in the literature. Major star-forming regions of NGC 6822 are heavily permeated with "RELIABLE" YSO candidates. The results of this study, in concert with those presented in Jones et al. (2019), imply the existence of three young, embedded star-forming clusters in the central region of NGC 6822 that have remained relatively unexplored. One such cluster, known as Spitzer I, is home to a greater number of YSO candidates than the galaxy's bright, well-known star-forming regions such as Hubble V. In this regard, Spitzer I may represent a proto-SSC in the early stages of its evolution, sharing interesting characteristics with the proto-SSC H72.97−69.39 found in the N79 region of the Large Magellanic Cloud (Ochsendorf et al. 2017; Nayak et al. 2019) and necessitating detailed follow-up study with dedicated observing time.

This project was developed in an effort to better understand the role that dust plays in star-forming systems with metal-poor environmental conditions analogous to those which populated the early universe. While the bulk of the enrichment history of the universe is traced to this epoch of peak star formation ($z \sim 1.5$–2), within these galaxies the low- to intermediate-mass MS stars would not have had sufficient time to reach the AGB phase of their evolution. As AGB stars are a primary producer of dust, a census of these evolved stars and study of their enrichment properties in extremely metal-poor environments is critical to understanding the early universe.

Future JWST GTO programs investigating the dusty and evolved star populations of metal-poor, early-universe analog systems will deliver high-quality observational data of NGC 6822 and the blue compact dwarf (BCD) galaxy I Zw 18. The near- and mid-IR wavelength coverage of the Near-Infrared Camera (NIRCam) and Mid-Infrared Instrument (MIRI) will provide photometry similar to those used in this study. Development of best practices are therefore of great importance for the upcoming JWST era, in which quick turnaround for spectral follow-up of interesting sources will be necessary.

The authors would like to thank the referee for the useful comments provided which helped to improve this paper. We thank Bernie Shiao for his assistance running CASJobs queries, which were used in developing the joined master catalog of photometric sources. We additionally extend our thanks to Owen Boberg and Peter Scicluna for their help with developing Python routines used in the source classifications. A.S.H. and M.M. acknowledge support from NASA grant NNX14AN06G. L.G. was funded via the Space Astronomy Summer Program (SASP) at STScI. Thanks to William Paranzino, a Johns Hopkins University summer intern, for his help in the early assessment of contaminants to the catalog. O.C.J. has received funding from the EUs Horizon 2020 programme under the Marie Sklodowska-Curie grant agreement No 665593 awarded to the STFC. This research made use of Astropy,[10] a community-developed core Python package for Astronomy (Astropy Collaboration et al. 2013); APLpy, an open-source plotting package for Python (Robitaille & Bressert 2012); and the SIMBAD database, operated at CDS, Strasbourg, France (Wenger et al. 2000).

ORCID iDs

Alec S. Hirschauer https://orcid.org/0000-0002-2954-8622
Laurin Gray https://orcid.org/0000-0001-6389-5639
Margaret Meixner https://orcid.org/0000-0002-0522-3743
Olivia C. Jones https://orcid.org/0000-0003-4870-5547
Sundar Srinivasan https://orcid.org/0000-0002-2996-305X
Martha L. Boyer https://orcid.org/0000-0003-4850-9589
B. A. Sargent https://orcid.org/0000-0001-9855-8261

References

Astropy Collaboration, Robitaille, T. P., Tollerud, E. J., et al. 2013, A&A, 558, A33
Baldacci, L., Matonti, F., Rizzi, L., et al. 2004, MmSAI, 75, 126
Battinelli, P., & Demers, S. 2005, A&A, 434, 657
Battinelli, P., & Demers, S. 2011, A&A, 525, A69
Bernard, J.-P., Reach, W. T., Paradis, D., et al. 2008, AJ, 136, 919
Bianchi, L., Scuderi, S., Massey, P., & Romaniello, M. 2001, AJ, 121, 2020
Blum, R. D., Mould, J. R., Olsen, K. A., et al. 2006, AJ, 132, 2034
Blum, R. D., Srinivasan, S., Kemper, F., et al. 2014, AJ, 148, 86
Boyer, M. L. 2019, in IAU Symp. 343, Why Galaxies Care About AGB Stars: A Continuing Challenge through Cosmic Time, ed. K. Kerschbaum, M. Groenewegen, & H. Olofsson (Cambridge: Cambridge Univ. Press), 321
Boyer, M. L., McDonald, I., Srinivasan, S., et al. 2015c, ApJ, 810, 116
Boyer, M. L., McQuinn, K. B. W., Barmby, P., et al. 2015a, ApJS, 216, 10
Boyer, M. L., McQuinn, K. B. W., Barmby, P., et al. 2015b, ApJ, 800, 51
Boyer, M. L., McQuinn, K. B. W., Groenewegen, M. A. T., et al. 2017, ApJ, 851, 152
Boyer, M. L., Srinivasan, S., Riebel, D., et al. 2012, ApJ, 748, 40
Boyer, M. L., Srinivasan, S., van Loon, J. T., et al. 2011, AJ, 142, 103
Bruzual, G., Charlot, S., López lira, R. G., et al. 2013, in IAU Symp. Ser. 295, The Intriguing Life of Massive Galaxies, ed. D. Thomas, A. Pasquali, & I. Ferreras (Cambridge: Cambridge Univ. Press), 282
Cannon, J. M., Walter, F., Armus, L., et al. 2006, ApJ, 652, 1170
Carlson, L. R., Sewiło, M., Meixner, M., Romita, K. A., & Lawton, B. 2012, A&A, 542, A66
Cioni, M.-R. L. 2009, A&A, 506, 1137

[10] http://www.astropy.org/

Cioni, M.-R. L., Girardi, L., Marigo, P., & Habing, H. J. 2006, A&A, 448, 77
Cioni, M.-R. L., & Habing, H. J. 2005, A&A, 429, 837
Cioni, M.-R. L., van der Marel, R. P., Loup, C., et al. 2000, A&A, 359, 601
Clementini, G., Held, E. V., Baldacci, L., & Rizzi, L. 2003, ApJL, 588, L85
Dalcanton, J. J., Williams, B. F., Seth, A. C., et al. 2009, ApJS, 183, 67
de Blok, W. J. G., & Walter, F. 2000, ApJL, 537, L95
de Blok, W. J. G., & Walter, F. 2006, AJ, 131, 343
Dell'Agli, F., García-Hernández, D. A., Ventura, P., et al. 2015, MNRAS, 454, 4235
Fazio, G. G., Hora, J. L., Allen, L. E., et al. 2004, ApJS, 154, 10
Freedman, W. L., Madore, B. F., Hatt, D., et al. 2019, ApJ, 882, 34
Galametz, M., Madden, S. C., Galliano, F., et al. 2010, A&A, 518, L55
Gallagher, J. S., III, Hunter, D. A., Gillett, F. C., & Rice, W. L. 1991, ApJ, 371, 142
Gallart, C., Aparicio, A., Chiosi, C., et al. 1994, ApJL, 425, L9
Gallart, C., Aparicio, A., & Vilchez, J. M. 1996, AJ, 112, 1928
Gardner, J. P., Mather, J. C., Clampin, M., et al. 2006, SSRv, 123, 485
Girardi, L., Barbieri, M., Groenewegen, M. A. T., et al. 2012, ASSP, 26, 165
Goldman, S. R., Boyer, M. L., McQuinn, K. B. W., et al. 2019, ApJ, 884, 152
Gordon, K. D., Meixner, M., Meade, M. R., et al. 2011, AJ, 142, 102
Gouliermis, D. A., Schmeja, S., Klessen, R. S., de Blok, W. J. G., & Walter, F. 2010, ApJ, 725, 1717
Gratier, P., Braine, J., Rodriguez-Fernandez, N. J., et al. 2010, A&A, 512, A68
Groenewegen, M. A. T. 2006, A&A, 448, 181
Groenewegen, M. A. T., Lançon, A., & Marescaux, M. 2009, A&A, 504, 1031
Henize, K. G. 1956, ApJS, 2, 315
Hernández-Martínez, L., & Peña, M. 2009, A&A, 495, 447
Hernández-Martínez, L., Peña, M., Carigi, L., & García-Rojas, J. 2009, A&A, 505, 1027
Hodge, P., Kennicutt, R. C., & Lee, M. G. 1988, PASP, 100, 917
Hodge, P., Lee, M. G., & Kennicutt, R. C. 1989, PASP, 101, 32
Hodgkin, S. T., Irwin, M. J., Hewett, P. C., & Warren, S. J. 2009, MNRAS, 394, 675
Hoessel, J. G., & Anderson, N. 1986, ApJS, 60, 507
Höfner, S., & Olofsson, H. 2018, A&AR, 26, 1
Holtzman, J. A., Afonso, C., & Dolphin, A. 2006, ApJS, 166, 534
Hubble, E. P. 1925, ApJ, 62, 409
Hunter, D. A., & Elmegreen, B. G. 2006, ApJS, 162, 49
Hunter, D. A., & Kaufman, M. 2007, AJ, 134, 721
Iben, I., Jr., & Renzini, A. 1983, ARA&A, 21, 271
Irwin, M. J., Lewis, J., Hodgkin, S., et al. 2004, Proc. SPIE, 5493, 411
Israel, F. P., Baas, F., Rudy, R. J., Skillman, E. D., & Woodward, C. E. 2003, A&A, 397, 87
Israel, F. P., Bontekoe, T. R., & Kester, D. J. M. 1996, A&A, 308, 723
Ivezić, Ž, Connelly, A. J., VanderPlas, J. T., et al. 2014, Statistics, Data Mining, and Machine Learning in Astronomy (Princeton, NJ: Princeton Univ. Press)
Jones, O. C., Maclay, M. T., Boyer, M. L., et al. 2018, ApJ, 854, 117
Jones, O. C., Meixner, M., Justtanont, K., & Glasse, A. 2017a, ApJ, 841, 15
Jones, O. C., Meixner, M., Sargent, B. A., et al. 2015, ApJ, 811, 145
Jones, O. C., Sharp, M. J., Reiter, M., et al. 2019, MNRAS, 490, 832
Jones, O. C., Woods, P. M., Kemper, F., et al. 2017b, MNRAS, 470, 3250
Kacharov, N., Rejkuba, M., & Cioni, M.-R. L. 2012, A&A, 537, A108
Kang, A., Sohn, Y.-J., Kim, H.-I., et al. 2006, A&A, 454, 717
Kemper, F., Woods, P. M., Antoniou, V., et al. 2010, PASP, 122, 683
Kennicutt, R. C. 1979, ApJ, 228, 394
Khan, R., Stanek, K. Z., & Kochanek, C. S. 2013, ApJ, 767, 52
Khan, R., Stanek, K. Z., Kochanek, C. S., & Sonneborn, G. 2015, ApJS, 219, 42
Khan, R., Stanek, K. Z., Prieto, J. L., et al. 2010, ApJ, 715, 1094
Kirby, E. N., Rizzi, L., Held, E. V., et al. 2017, ApJ, 834, 9
Komiyama, Y., Okamura, S., Yagi, M., et al. 2003, ApJL, 590, L17
Lee, H., Skillman, E. D., & Venn, K. A. 2006, ApJ, 642, 813
Lee, J.-K., Rolleston, W. R. J., Dufton, P. L., & Ryans, R. S. I. 2005, A&A, 429, 1025
Lee, S., Pak, S., Lee, S.-G., et al. 2005, MNRAS, 361, 1273
Letarte, B., Demers, S., Battinelli, P., & Kunkel, W. E. 2002, AJ, 123, 832
Madau, P., & Dickinson, M. 2014, ARA&A, 52, 415
Madore, B. F., Freedman, W. L., Hatt, D., et al. 2018, ApJ, 858, 11
Marconi, G., Tosi, M., Greggio, L., et al. 1995, AJ, 109, 173
Marengo, M., Hora, J. L., Barmby, P., et al. 2007, in ASP Conf. Ser. 378, Why Galaxies Care About AGB Stars, Their Importance as Actors and Probes 80, ed. F. Kerschbaum, C. Charbonnel, & R. F. Wing (San Francisco, CA: ASP), 80
Marigo, P., Bressan, A., Nanni, A., Girardi, L., & Pumo, M. L. 2013, MNRAS, 434, 488
Marigo, P., Girardi, L., & Bressan, A. 1999, A&A, 344, 123
Marigo, P., Girardi, L., Bressan, A., et al. 2008, A&A, 482, 883
Marigo, P., Girardi, L., & Chiosi, C. 2003, A&A, 403, 225
Massey, P., Armandroff, T. E., Pyke, R., Patel, K., & Wilson, C. D. 1995, AJ, 110, 2715
Massey, P., Olsen, K. A. G., Hodge, P. W., et al. 2007, AJ, 133, 2393
Matsuura, M., Barlow, M. J., Zijlstra, A. A., et al. 2009, MNRAS, 396, 918
McConnachie, A. W. 2012, AJ, 144, 4
McQuinn, K. B. W., Boyer, M. L., Mitchell, M. B., et al. 2017, ApJ, 834, 78
Meixner, M., Galliano, F., Hony, S., et al. 2010, A&A, 518, L71
Meixner, M., Gordon, K. D., Indebetouw, R., et al. 2006, AJ, 132, 2268
Meixner, M., Panuzzo, P., Roman-Duval, J., et al. 2013, AJ, 146, 62
Melena, N. W., Elmegreen, B. G., Hunter, D. A., & Zernow, L. 2009, AJ, 138, 1203
Nayak, O., Meixner, M., Sewiło, M., et al. 2019, ApJ, 877, 135
Nikolaev, S., & Weinberg, M. D. 2000, ApJ, 542, 804
O'Dell, C. R., Hodge, P. W., & Kennicutt, R. C. 1999, PASP, 111, 1382
Ochsendorf, B. B., Zinnecker, H., Nayak, O., et al. 2017, NatAs, 1, 784
Riebel, D., Srinivasan, S., Sargent, B., et al. 2012, ApJ, 753, 71
Rieke, G. H., Young, E. T., Engelbracht, C. W., et al. 2004, ApJS, 154, 25
Robitaille, T., & Bressert, E. 2012, APLpy: Astronomical Plotting Library in Python, v.2.0.3, Astrophysics Source Code Library, ascl:1208.017
Rolleston, W. R. J., Dufton, P. L., McErlean, N. D., & Venn, K. A. 1999, A&A, 348, 728
Rolleston, W. R. J., Venn, K., Tolstoy, E., & Dufton, P. L. 2003, A&A, 400, 21
Rubin, R. H., Simpson, J. P., Colgan, S. W. J., et al. 2016, MNRAS, 459, 1875
Ruffle, P. M. E., Kemper, F., Jones, O. C., et al. 2015, MNRAS, 451, 3504
Russell, S. C., & Dopita, M. A. 1992, ApJ, 384, 508
Sakai, S., Madore, B. F., & Freedman, W. L. 1996, ApJ, 461, 713
Salaris, M., & Girardi, L. 2005, MNRAS, 357, 669
Sandstrom, K. M., Bolatto, A. D., Bot, C., et al. 2012, ApJ, 744, 20
Schlegel, D. J., Finkbeiner, D. P., & Davis, M. 1998, ApJ, 500, 525
Schruba, A., Leroy, A. K., Kruijssen, J. M. D., et al. 2017, ApJ, 835, 278
Seale, J. P., Looney, L. W., Chu, Y.-H., et al. 2009, ApJ, 699, 150
Seale, J. P., Meixner, M., Sewiło, M., et al. 2014, AJ, 148, 124
Sewiło, M., Carlson, L. R., Seale, J. P., et al. 2013, ApJ, 778, 15
Sibbons, L. F., Ryan, S. G., Cioni, M.-R. L., Irwin, M., & Napiwotzki, R. 2012, A&A, 540, A135
Sibbons, L. F., Ryan, S. G., Napiwotzki, R., & Thompson, G. P. 2015, A&A, 574, A102
Skillman, E. D., Terlevich, R., & Melnick, J. 1989, MNRAS, 240, 563
Srinivasan, S., Boyer, M. L., Kemper, F., et al. 2016, MNRAS, 457, 2814
Van Sistine, A., Salzer, J. J., Sugden, A., et al. 2016, ApJ, 824, 25
Weinberg, M. D., & Nikolaev, S. 2001, ApJ, 548, 712
Wenger, M., Ochsenbein, F., Egret, D., et al. 2000, A&AS, 143, 9
Werner, M. W., Roellig, T. L., Low, F. J., et al. 2004, ApJS, 154, 1
Whitelock, P. A., Menzies, J. W., Feast, M. W., Nsengiyumva, F., & Matsunaga, N. 2013, MNRAS, 428, 2216
Whitney, B. A., Sewilo, M., Indebetouw, R., et al. 2008, AJ, 136, 18
Woods, P. M., Oliveira, J. M., Kemper, F., et al. 2011, MNRAS, 411, 1597
Wright, N. J., Barlow, M. J., Greimel, R., et al. 2009, MNRAS, 400, 1413
Yang, M., Bonanos, A. Z., Jiang, B.-W., et al. 2018, A&A, 616, A175
Yang, M., Bonanos, A. Z., Jiang, B.-W., et al. 2019, A&A, 629, A91